



HAL
open science

Impact of microwave beam scattering by density fluctuations on the electron–cyclotron power deposition profile in tokamaks

J. Cazabonne, S. Coda, J. Decker, O. Krutkin, U. Kumar, Y. Peysson

► **To cite this version:**

J. Cazabonne, S. Coda, J. Decker, O. Krutkin, U. Kumar, et al.. Impact of microwave beam scattering by density fluctuations on the electron–cyclotron power deposition profile in tokamaks. *Nuclear Fusion*, 2024, 64 (2), pp.026019. 10.1088/1741-4326/ad1af6 . cea-04816345

HAL Id: cea-04816345

<https://cea.hal.science/cea-04816345v1>

Submitted on 3 Dec 2024





HAL is a multi-disciplinary open access archive for the deposit and dissemination of scientific research documents, whether they are published or not. The documents may come from teaching and research institutions in France or abroad, or from public or private research centers.

L'archive ouverte pluridisciplinaire **HAL**, est destinée au dépôt et à la diffusion de documents scientifiques de niveau recherche, publiés ou non, émanant des établissements d'enseignement et de recherche français ou étrangers, des laboratoires publics ou privés.



Distributed under a Creative Commons Attribution 4.0 International License

Impact of microwave beam scattering by density fluctuations on the electron–cyclotron power deposition profile in tokamaks

J. Cazabonne^{1,*} , S. Coda¹ , J. Decker¹, O. Krutkin¹ , U. Kumar¹ , Y. Peysson² and the TCV Team^{1,a}

¹ École Polytechnique Fédérale de Lausanne (EPFL), Swiss Plasma Center (SPC), CH-1015 Lausanne, Switzerland

² CEA, IRFM, Saint-Paul-Lez-Durance F-13108, France

E-mail: jean.cazabonne@epfl.ch

Received 16 October 2023, revised 13 December 2023

Accepted for publication 4 January 2024

Published 16 January 2024



Abstract

Electron–cyclotron waves are a tool commonly used in tokamaks, in particular to drive current. Their ability to drive current in a very localized manner renders them an optimal tool for MHD mode mitigation. However, such applications require high accuracy and good control of the power deposition location to efficiently target the magnetic islands. It has been indirectly observed that the suprathermal electron distribution, resulting from the wave absorption, is broader than what is expected from experimentally-constrained forward drift-kinetic modeling. The present paper explores the possibility that beam scattering through the turbulent edge of the plasma may explain this observed discrepancy. In particular, full-wave studies exhibit three beam broadening regimes, from superdiffusive to diffusive, with an intermediate regime characterized by a Lorentzian beam profile with a slightly increased full-width at half maximum with respect to the quiet plasma case. In the tokamak à configuration variable, dedicated plasma scenarios have been developed to test this hypothesis. A realistic worst-case fluctuation scenario falls into this intermediate beam broadening regime. By comparing the experimental hard x-ray emission from suprathermal electron Bremsstrahlung with the emission calculated by coupling a full-wave model to a Fokker–Planck solver, it is shown that, in the tested cases, the beam broadening is not sufficient to explain the aforementioned discrepancy between simulation and experiment and that another mechanism must play the main role in broadening the suprathermal electron distribution.

^a See Reimerdes *et al* 2022 (<https://doi.org/10.1088/1741-4326/ac369b>) for the TCV Team.

* Author to whom any correspondence should be addressed.



Original Content from this work may be used under the terms of the [Creative Commons Attribution 4.0 licence](https://creativecommons.org/licenses/by/4.0/). Any further distribution of this work must maintain attribution to the author(s) and the title of the work, journal citation and DOI.

Keywords: tokamak, electron–cyclotron, hard x-ray spectrometry, density fluctuations, beam scattering, Fokker–Planck simulations

(Some figures may appear in colour only in the online journal)

1. Introduction

Electron–Cyclotron (EC) waves are widely used in the tokamak community to heat the plasma and to drive current, taking advantage of the resonant energy transfer from the wave to the plasma, via the cyclotron motion of electrons. The short wavelength and excellent directionality of these waves result in a high degree of accuracy in the spatial localization of the power deposition [1]. Depending on the EC wave vector component parallel to the main magnetic field k_{\parallel} , it is possible to solely increase the electron temperature using the so-called EC Resonant Heating (ECRH, $k_{\parallel} = 0$) or to drive current by Doppler shifting the resonance in velocity space. This results in an asymmetric distortion of the electron distribution function, using the EC Current Drive configuration (ECCD, $k_{\parallel} \neq 0$). This ability to drive current locally and to shape the current profile renders the ECCD the primary foreseen tool for the mitigation of magneto-hydro-dynamic (MHD) instabilities, such as Neoclassical Tearing Mode (NTM), in future large fusion devices. The principle of MHD mitigation is to drive current into the magnetic islands, which requires precise knowledge of the plasma position as well as of the power deposition location [2]. However, it has been observed that the radial distribution of suprathermal electrons, resulting from the EC wave absorption accelerating electrons to suprathermal velocities, is broader than expected from ray-tracing and drift-kinetic simulations [3, 4]. This broadening can hamper the accuracy of the EC power deposition localization, and the underlying mechanisms must be understood to improve the predictive capabilities of the numerical tools. Recent work on DIII-D [5] has shown that the experimentally reconstructed EC power deposition profile is broader than the one obtained using forward ray-tracing modeling by a factor 1.6–3.6. This study also concludes that, in ITER, full NTM suppression will be achievable only for a broadening factor of the power deposition profile less than 2.4, considering the available EC power.

A first mechanism proposed to understand the discrepancy between experimental observations and drift-kinetic simulations is the increase of the radial transport of suprathermal electrons induced by the EC wave [3]. This has been suggested by EC power modulation experiments performed on the Tokamak à Configuration Variable (TCV, major radius $R = 0.89$ m, minor radius $a = 0.25$ m, magnetic field $B_0 \sim 1.5$ T) [6], coupled with drift-kinetic forward modeling using ad-hoc transport models, concluding that the radial transport of electrons should be proportional to the phase-space-localized EC wave deposited power to recover the experimental data [7]. This ad-hoc transport has been correlated experimentally as well as numerically with an increase of turbulent transport with EC power, related to Trapped Electron Modes (TEMs) or Ion Temperature Gradient (ITG), in a

stiff electron temperature profile configuration [8]. This work uses drift-kinetic simulations, but also first principles flux-driven gyro-kinetic simulations, benefiting from the development of a realistic EC power source in the gyro-kinetic code ORB5 [9, 10].

A second possible explanation, which does not exclude the first one, is the scattering of the EC beam passing through the fluctuating plasma refractive index before its absorption. This scattering results in an average beam broadening that may affect the power deposition profile. Analytical and numerical work has been performed to better understand this broadening effect, using different approaches such as quasi-optics [11–13], statistical Fokker–Planck formalism [14, 15], ray tracing coupled to a drift-kinetic Fokker–Planck solver [16–18], wave-kinetic equation solver [19] benchmarked against full-wave simulations [20–22], proper full-wave simulations in tokamak-relevant conditions [23], or simulations of the effect of single-blob [24] and multi-blob [25] density structures on a microwave beam. These numerical studies tend to conclude that the effect of wave scattering on the beam broadening may be important, particularly in large-sized tokamak like ITER or DEMO, where the wave travels over a distance of meters before reaching the absorption location. Quantifying this effect is still challenging, as it highly depends on the properties of the density fluctuations. For the ITER equatorial launchers in the baseline H-mode scenario, one can expect from 20% to 150% of beam broadening [21]. A multi-model approach has also been proposed to study NTM mitigation using EC waves in a turbulent plasma, concluding that, for ITER-relevant configurations, the damping time of the NTM is up to four times longer in the presence of edge-localized density blobs because of the turbulence-induced beam refraction and diffraction [26]. Part of these studies focus mainly on the beam broadening but not on the resulting power deposition profile, which also depends on the wave injection configuration.

Recently, effort has been placed in the experimental characterization of the impact of edge-localized density fluctuations on the beam broadening. Experimental studies on the toroidal device TORPEX [27] and on TCV [28, 29] in the case of non-absorbed, fully-transmitted microwave beam, with the support of a full-wave propagation solver, have shown a correlation between the transmitted EC power and the density fluctuations. In TCV specifically, it has been related to a combination of Scrape-Off Layer (SOL) turbulence, using experimentally validated fluid simulations performed with the Global Braginskii Solver (GBS) code [28], and core turbulence calculated by gradient-driven gyro-kinetic simulations [29]. It was shown that core turbulence, even though of relatively lower amplitude than edge turbulence, can account for up to 50% of the measured transmitted power deposition broadening. In

DIII-D, the beam broadening has been experimentally evidenced by analyzing the temperature perturbation induced by the EC beam, fitting the heat transport with a model taking into account the beam width, estimated through a full-wave model [30–32]. In that case, edge density fluctuations have been characterized using both beam emission spectroscopy measurements and fluid simulations [32].

The present paper explores the phenomenon of EC beam broadening and its impact on the power deposition profile, both numerically and experimentally. In particular, we investigate whether beam broadening can explain the discrepancy between the Hard X-Ray (HXR) measurements, from supra-thermal electron Bremsstrahlung emission, and the results given by drift-kinetic Fokker-Planck simulations for TCV. The modeling and the density fluctuation measurement technique are introduced in section 2. Then, in section 3, the different numerical tools used in this work are presented. A purely numerical study is detailed in section 4, using TCV-like analytical equilibria and scanning the fluctuation parameters, with the aim of identifying the most probable beam broadening scenario in TCV, as well as a worst-case scenario. Finally, in section 5, experimental results are compared with simulations, using worst-case-scenario but realistic fluctuation parameters.

2. Density fluctuation measurement and modeling

In a turbulent plasma, the electron density can be written as $n_e(\rho_{\psi_p}, \theta) = \bar{n}_e(\rho_{\psi_p}) + \delta n_e(\rho_{\psi_p}, \theta)$ in the poloidal coordinate system (ρ_{ψ_p}, θ) , where \bar{n}_e is the averaged profile and δn_e the fluctuating part. In TCV, the profile of the Root-Mean-Square (RMS) relative density fluctuation level $[\delta n_e / \bar{n}_e]_{RMS}$ can be measured by Short-Pulse Reflectometry (SPR) [33]. The SPR diagnostic sends short pulses or wave-trains (≤ 1 ns) at varying microwave frequencies (50 GHz to 75 GHz), with a pulse repetition rate of 8.33 MHz in either O- or X-polarization. Upon encountering the cut-off, the pulse reflects back to the SPR receiver. The returned pulse is then recorded using an Analog-to-Digital Converter (ADC) with a sampling rate of 32 Gsamples s^{-1} . The statistical properties of the group delays are analyzed to infer information about the plasma density fluctuations: in particular, the RMS fluctuation level can be inferred from the RMS value of the delays [34]. For O-mode waves, the cutoff depends only on the plasma density, so the analysis of the reflected pulse delay gives direct information on the position of a given density layer (the pulse shape is fitted with a Gaussian to ensure a good estimate of the pulse delay is provided). X-mode polarization is used to probe the edge of the plasma as it is reflected at lower plasma density than O-mode. However, the analysis is more challenging as the cutoff for X-mode depends on both the plasma density and the magnetic field. A poloidal view of the plasma area probed by the SPR for a relevant TCV shot used in this study is shown in figure 1.

Simulations are performed using random 2D fluctuating density profiles, generated by an analytical model, developed

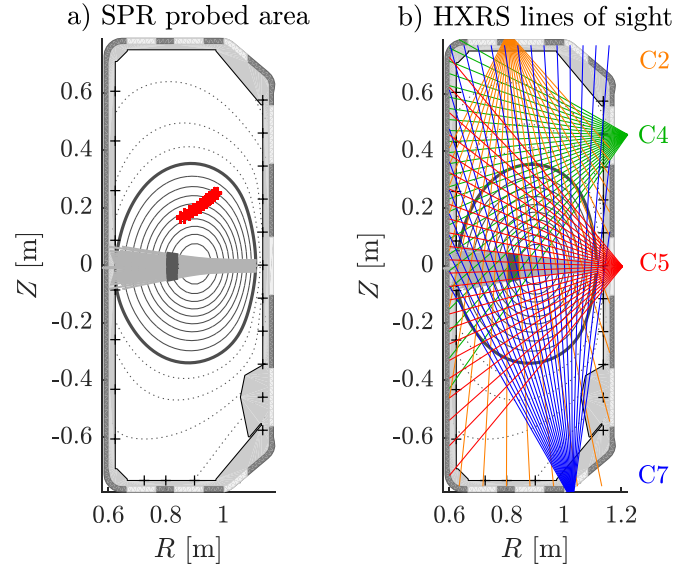


Figure 1. Poloidal view showing the plasma area (in red) probed by the Short Pulse Reflectometer (SPR) for TCV shot #77460 (a) and lines of sight of the four cameras (C2, C4, C5 and C7) of the Hard X-Ray Spectrometer (HXRS) (b).

in a drift-wave theoretical framework [16, 17]. The beam propagation being much faster than the evolution of the turbulence, density fluctuations are assumed to be frozen with respect to beam propagation. The model consists of a truncated Fourier series of Gaussian modes, convoluted with a 1D spatial envelope $F_{\Delta}(\rho_{\psi_p})$. The turbulent density structures are assumed to be toroidally homogeneous (blob-like). Since, in TCV, the toroidal extent of the EC beam at the edge is rather small (beam width of the order of 2 cm compared to an edge major radius of 1.12 m, meaning a toroidal extent of $\phi \simeq 1^\circ$), the helicity of the magnetic field, and so of the edge-localized field-aligned density blobs, is neglected in this model. This model gives for each independent time step

$$\begin{aligned} \frac{\delta n_e}{\bar{n}_e}(\rho_{\psi_p}, \theta, t) = F_{\Delta}(\rho_{\psi_p}) & \left[2\sigma_f \pi^{1/4} \sqrt{\frac{L_f}{L_c(\rho_{\psi_p})}} \right. \\ & \times \sum_{p=1}^{p_{\max}} \exp\left(-\frac{\pi^2}{2} \left(\frac{L_f}{L_c(\rho_{\psi_p})}\right)^2 p^2\right) \\ & \left. \times \sin(\Phi_p(\rho_{\psi_p}, \theta, t)) \right] \end{aligned} \quad (1)$$

where p is the mode number, σ_f is a parameter controlling the RMS of the density fluctuation level $[\delta n_e / \bar{n}_e]_{RMS}$, L_f is the characteristic size of the turbulent structures, Φ_p is a random phase defined by

$$\Phi_p(\psi_p, \theta, t) = p\vartheta(\psi_p, \theta) + 2\pi\chi_p(t) \quad (2)$$

with χ_p a random number ranging between 0 and 1 and ϑ an angle describing the drift wave poloidal structure, satisfying

the relations $\mathbf{B} \cdot \nabla \vartheta = 0$ and $\nabla \psi_P \cdot \nabla \vartheta = 0$. The characteristic length L_c is given by

$$L_c(\psi_P) = \frac{1}{q(\psi_P)} \int_0^{2\pi} r(\psi_P, \theta) \frac{B(\psi_P, \theta)}{B_\phi(\psi_P, \theta)} \frac{d\theta}{\cos(\alpha(\psi_P, \theta))} \quad (3)$$

where B and B_ϕ are the total and toroidal magnetic fields respectively, r is the minor radius, q is the safety factor and α the metric angle accounting for non-circular magnetic flux surfaces. Only dominant modes up to p_{\max} are considered, with the limit set by

$$p_{\max} = \frac{\sqrt{-2 \ln \beta} L_c(\psi_P)}{\pi L_f} \quad (4)$$

with β the minimum amplitude of the mode.

Different shapes can be assumed for the 1D spatial envelope F_Δ , which is fitted to the SPR experimental data, parameterized by the Half-Width at Half Maximum (HWHM) Δ , the RMS fluctuation level at the edge $[\delta n_e / \bar{n}_e]_{\text{RMS},1}$ and the background RMS fluctuation level $[\delta n_e / \bar{n}_e]_{\text{RMS},0}$. In TCV, measurements with the SPR diagnostic are limited to $\rho_{\psi_P} \leq 0.95$ for the studied scenarios, and it is very challenging to extrapolate data at the separatrix and in the outer edge, as the density fluctuation level is expected to sharply increase with radius. This behavior was already experimentally shown in the TEXT tokamak [35] and later confirmed by experiments in TCV [36, 37] and in ASDEX Upgrade [38], among others. This tendency is also observed in fluid simulations of the plasma edge, such as in TCV [29] or in DIII-D [32]. In particular, it has been shown in TCV, using a fast reciprocating Langmuir probe on the plasma equatorial midplane, that the relative RMS level of density fluctuation sharply increases toward the edge, saturating in the SOL at $[\delta n_e / \bar{n}_e]_{\text{RMS},\text{SOL}} = 60 \pm 10\%$ for a wide range of plasma scenarios [36, 37]. Given the uncertainties on its determination, the parameter $[\delta n_e / \bar{n}_e]_{\text{RMS},1}$ has to be scanned over a realistic range to assess the potential impact of edge density fluctuations on the EC beam and power deposition broadening in actual experiments.

The expected typical size of turbulent structures is $L_f \sim 5-10 \rho_{L,s}$, with $\rho_{L,s}$ the sonic Larmor radius defined by $\rho_{L,s} = c_s / \Omega_{c,i}$ where the sound speed is $c_s = \sqrt{k_B T_e / m_i}$ and the ion cyclotron frequency is $\Omega_{c,i} = q_i B / m_i$. It has been shown in DIII-D that, for L-mode plasmas, the edge density fluctuation correlation length scales as $L_f \sim 5-10 \rho_{L,s}$, by comparing experimental measurements from reflectometry and gyrokinetic simulations of ITG modes [39]. In the linear magnetized plasma of the LAPD machine, density blob analysis using Langmuir probes shows that the typical blob size scales around $10 \rho_{L,s}$ [40]. Finally, fluid simulations of TCV L-mode discharges using the GBS code found a correlation length of $7.4 \rho_{L,s}$ in the SOL [41].

Ultimately, the goal of this study is to test whether the EC beam scattering through the turbulent plasma can explain the discrepancy between simulations and experiments, so the most

interesting cases are the worst-case scenarios. This translates to ion-scale, high-amplitude density fluctuations. This will be discussed further in section 4.

3. Numerical tools for wave propagation and absorption, and for comparison with experiments

EC wave propagation and absorption in tokamaks can be simulated in many different ways, using tools such as ray-tracing codes (e.g. C3PO [18]), paraxial beam-tracing codes (e.g. TORBEAM [42, 43]), complex eikonal beam-tracing codes (e.g. GRAY [44]), wave-kinetic solvers (e.g. WKBBeam [19]) and full-wave codes (e.g. IPF-FDMC [45] or EMIT-3D [46]), each having their strengths and their limitations. An overview and a benchmark of different ray-tracing, beam-tracing and quasi-optical codes for an ITER configuration can be found in [47], and in [48] for European codes. Two different and complementary approaches are used in the present paper to propagate the EC beam: full-wave and ray-tracing, while the EC beam quasilinear absorption is treated in a drift-kinetic Fokker-Planck solver.

3.1. Full-wave finite elements COMSOL solver

The Radio-Frequency module of COMSOL Multiphysics® [49] (hereafter referred to simply as COMSOL) provides a finite-element solver allowing the resolution of the full-wave equation governing the evolution of the EC beam electric field in Fourier space $\tilde{\mathbf{E}}(\mathbf{x}, \omega)$

$$\nabla \times (\nabla \times \tilde{\mathbf{E}}(\mathbf{x}, \omega)) - \frac{\omega^2}{c^2} \bar{\epsilon}(n_e(\mathbf{x}), B(\mathbf{x}), \omega) \tilde{\mathbf{E}}(\mathbf{x}, \omega) = \mathcal{S} \quad (5)$$

with ω the beam frequency, \mathbf{x} the position vector, \mathcal{S} a source term and $\bar{\epsilon}$ the plasma dielectric tensor. The dielectric tensor is reduced to its Hermitian part $\bar{\epsilon}_H$ ($\epsilon_{H,ij} = \bar{\epsilon}_{H,ji}$), so the model is limited to treating the EC beam propagation, but not its absorption (no dissipation effects are included) [50]. Thermal effects appears at first order only close to the resonance, which is very localized in space for a Low-Field Side (LFS) EC beam launching configuration. In that case, the propagation of an EC wave can be efficiently modeled with the cold plasma dielectric tensor [1, 51]. This approximation may not be valid for EC waves launched along the resonant layer.

The cold plasma dielectric tensor for a general magnetic field in Cartesian coordinates has been derived and implemented in COMSOL and reads [28, 29]

$$\bar{\epsilon}_H = \begin{pmatrix} S(1 - b_1^2) + P b_1^2 & +i D b_3 + Q b_1 b_2 & -i D b_2 + Q b_1 b_3 \\ -i D b_3 + Q b_2 b_1 & S(1 - b_2^2) + P b_2^2 & +i D b_1 + Q b_2 b_3 \\ +i D b_2 + Q b_3 b_1 & -i D b_1 + Q b_3 b_2 & S(1 - b_3^2) + P b_3^2 \end{pmatrix} \quad (6)$$

where b_1 , b_2 and b_3 are the normalized components of the magnetic field in an arbitrary Cartesian coordinate system, and P , S , D and Q are the Stix coefficients [52]

$$\begin{aligned}
P &= 1 - \frac{\omega_{p,e}^2}{\omega^2} & ; & \quad S = 1 - \frac{\omega_{p,e}^2}{\omega^2 - \Omega_{c,e}^2} \\
D &= \frac{\Omega_{c,e}}{\omega} \frac{\omega_{p,e}^2}{\omega^2 - \Omega_{c,e}^2} & ; & \quad Q = P - S = \frac{\Omega_{c,e}^2}{\omega^2 - \Omega_{c,e}^2}
\end{aligned} \quad (7)$$

with the plasma frequency $\omega_{p,e} = \sqrt{n_e e^2 / (\epsilon_0 m_e)}$ and the electron cyclotron frequency $\Omega_{c,e} = eB/m_e$. The computational cost of such simulations limits the calculation to 2D configuration only. So only ECRH and 2D ECCD can be treated (e.g. ECCD beam propagating on the equatorial midplane). This high computational cost is partly due to the fact that a mesh size such that $L_{\text{mesh}} \leq \lambda_0/5$ is necessary to avoid numerical diffraction of the beam by the mesh itself [28]. The source term in equation (5) is set to a Gaussian electric field at the EC beam launcher position, corresponding to the initial EC beam profile. For a Gaussian beam, the norm of the electric field is $|E(s_{\parallel}, s_{\perp})| = E_0 (w_0/w(s_{\parallel})) \exp(-s_{\perp}^2/w(s_{\parallel})^2)$ where w_0 is the beam waist, s_{\parallel} is the distance from the beam waist position along the beam propagation direction and s_{\perp} is the distance from the beam center in the transverse direction, $w(s_{\parallel})$ is the beam width and E_0 is the electric field amplitude at the beam waist position.

3.2. Ray-tracing C3PO code

Ray tracing is a very common tool for calculating wave propagation and linear absorption as it is fast and flexible and is often coupled to other codes that need at least an EC wave propagation solver, such as drift-kinetic Fokker-Planck solver (e.g. LUKE [53]). The ray-tracing code C3PO [18] solves the following Hamiltonian system to propagate the optical ray

$$\begin{aligned}
\frac{d\mathbf{X}}{dt} &= -\frac{\partial \mathcal{D}}{\partial \mathbf{k}} / \frac{\partial \mathcal{D}}{\partial \omega} \\
\frac{d\mathbf{k}}{dt} &= \frac{\partial \mathcal{D}}{\partial \mathbf{X}} / \frac{\partial \mathcal{D}}{\partial \omega}
\end{aligned} \quad (8)$$

where \mathbf{X} is the position vector of the ray, \mathbf{k} is the wave vector and \mathcal{D} is the Hermitian part of the dispersion relation, the anti-Hermitian part being related to wave absorption. These six ordinary differential equations are then solved using the Runge–Kutta–Fehlberg method, making the calculation fast and adapted to the tokamak geometry. However, contrary to full-wave codes, the solver relies on the Wentzel–Kramers–Brillouin (WKB) approximation that constraints the ordering of the different characteristic lengths. The equilibrium characteristic length L_{eq} , the equilibrium inhomogeneity or fluctuation characteristic length L_f and the beam wavelength λ_0 must satisfy the following ordering:

$$L_{eq} \gg L_f \gg \lambda_0. \quad (9)$$

This may be an issue when considering edge density fluctuations as L_f scales as $1-10 \rho_{L,s}$, meaning that it is possible to have $L_f \sim \lambda_0$ (order of millimeters).

In C3PO, the total beam power is evenly spread between several power tubes, so-called beamlets, each carrying the

same fraction of the total power. The beamlets are radially and azimuthally spread around the central ray, and the distance between the beamlets and the central ray is constrained by the width of the beam power profile (proportional to the square of its electric field). Indeed, the radial spreading of the beamlets is such that the radial power density corresponds to either a Gaussian or a Lorentzian beam profile. Different modes are available: it is possible to estimate the Gaussian beam width along the propagation direction using Gaussian beam theory, taking into account the plasma refractive index and the poloidal curvature of magnetic flux surfaces (but only in the case of a quiet plasma) [54], or to input a custom Gaussian or Lorentzian beam width. This physical Gaussian beam implementation is still different from those of beam tracing and full-wave codes as the beam power profile is discrete and only refraction and small diffraction are treated but no higher order of diffusion, such as scattering. Indeed, this Gaussian beam model is developed within the paraxial approximation, meaning that the beam width must be much smaller than the characteristic diffraction length [55]. It is also developed within the WKB approximation, implying that the characteristic space scale of the beam width variation must be much greater than the beam wavelength. On the other hand, the custom mode enables the treatment of absorption for a beam propagated by the full-wave COMSOL model. All LUKE-C3PO simulations presented in this paper have been performed using this custom beam width model using inputs from COMSOL.

3.3. Bounce-averaged drift-kinetic LUKE for quasilinear wave absorption and comparison with Hard X-Ray Spectrometer (HXRS)

The drift-kinetic Fokker-Planck code LUKE [53] solves the bounce-averaged linearized Fokker–Planck equation, yielding the electron distribution function f_e . This equation reads

$$\frac{\partial f_e}{\partial t} = \sum_s \mathcal{C}(f_e, f_s) + \sum_n \mathcal{Q}_{EC,n}(f_e) + \mathcal{E}(f_e) \quad (10)$$

where $\mathcal{C}(f_e, f_s)$ is the operator describing collisions between electrons and species s . In TCV, those species are other electrons, the main deuterium ions and carbon VI+ impurities. LUKE only computes the electron distribution function so, for species other than electrons, f_s is considered to be Maxwellian in the collision operator. The operator $\mathcal{E}(f_e)$ describes the Ohmic electric field and the operator $\mathcal{Q}_{EC,n}(f_e)$ the quasilinear diffusion related to the wave-plasma interaction for each harmonics n . LUKE is directly coupled to C3PO, which solves the wave propagation and provides an initial guess of the wave power deposition. The quasilinear wave power deposition is then calculated iteratively, as the electron distribution is affected by the wave power deposition, which is, in turn, affected by the electron distribution. In this paper, LUKE calculations are performed in the time-asymptotic mode, meaning that the electric field is imposed by the measured loop voltage at the edge, assuming that the wave-induced electric field has completely diffused.

LUKE calculations are interesting for the present study for two main reasons: the possibility of estimating the power deposition resulting from COMSOL full-wave propagation by using the custom beam width mode of C3PO (later referred to as COMSOL-LUKE simulations), and the ability to compare simulation results directly with TCV experimental data. Such comparisons are enabled by the R5-X2 module of the LUKE suite [56], which computes the fast electron Bremsstrahlung from the non-thermal electron distribution function, and is used as a synthetic diagnostic for the TCV HXRS [57]. The HXRS consists of a set of four compact cameras, each possessing 24 cadmium telluride photodiodes, with a tungsten collimator defining the lines of sight, measuring the HXR count rate from suprathermal electron Bremsstrahlung (20–200 keV range, with 8 keV resolution). The count rate is sorted by energy bins using optimized digital pulse processing [58]. The complete set covers a total poloidal section of the tokamak. The synthetic diagnostic uses an experiment-based model of the cadmium telluride response function to estimate the line-integrated hard x-ray count rate that can be directly compared to the HXRS data [59]. A poloidal display of the HXRS lines of sight is shown in figure 1.

4. Full-wave numerical studies and beam broadening regimes: identifying a worst-case scenario

To assess the possible impact of turbulent density on the EC beam broadening in the TCV configuration, a purely numerical study is performed for a wide range of turbulent parameters. Three analytic equilibria are generated, using the solution to the Grad–Shafranov equation provided in [60]. The main parameters for these equilibria are summarized in table 1. The fluctuation patterns are generated using equation (1), enveloped by a 1D Gaussian centered around the Last Closed Flux Surface (LCFS) $F_\Delta = \exp(-[\rho_{\psi p} - 1]/\Delta)^2$. The main parameters controlling the density fluctuations are the amplitude σ_f , the envelope HWHM Δ and the characteristic size of the fluctuations L_f . The EC beam is a 82.7 GHz (3.625 mm vacuum wavelength) X-polarized beam, launched from the LFS in an ECRH configuration. In such a configuration, the beam is nearly fully-absorbed at the second harmonic resonance location (confirmed by C3PO ray-tracing calculation). To simulate a turbulent plasma, the EC beam is propagated through 100 individual and independent fluctuating density snapshots (assuming that the beam propagates much faster than the fluctuation correlation time), using the full-wave COMSOL model. The beam electric field is then averaged over the snapshots, yielding the average impact of edge-localized density fluctuation on its broadening. The number of snapshots is enough for the width and position of the averaged EC beam to converge (at least before the absorption location). The beam electric field profile transverse to its propagation direction is then fitted with both Gaussian and Lorentzian shapes, so that the best fit is used to build a custom beam

width input for the COMSOL-LUKE simulations, which then calculates the quasilinear absorption. To illustrate the methodology, examples of an EC beam computed with COMSOL in a quiet plasma and in a turbulent plasma, both time-averaged and instantaneous, are shown in figure 2, together with the associated EC beam profiles taken just before the wave absorption location. The different scans in fluctuation parameters are summarized in table 2.

Beam scattering through a turbulent layer can be associated with different broadening regimes [20]. These regimes can be characterized within the framework of the wave-kinetic theory, considering the mode conversion of a wave by conservative momentum transfer with fluctuations: it is a three-wave coupling scenario involving the incident beam, the scattered beam and density fluctuations. Writing the three-wave coupling equations yields a microscopic scattering cross-section, which is then integrated over the refractive index space and modes to give a macroscopic scattering cross-section Σ_X . Finally, the average number of scattering events λ_X is estimated by integrating this macroscopic cross-section along the beam path, or is simplified considering $\lambda_X = \langle \Sigma_X \rangle [\Delta s_{\parallel}]_f$, with $\langle \Sigma_X \rangle$ the macroscopic scattering cross-section averaged over the beam path and $[\Delta s_{\parallel}]_f$ the width of the turbulent layer crossed by the beam. For X-polarization, the simplified version of λ_X can be written as [20]

$$\lambda_X \simeq \sqrt{\frac{\pi}{2}} \frac{1}{N_{\perp,X}} \left(\frac{\omega}{\omega + \Omega_{c,e}} \right)^2 \left[\frac{\delta n_e}{n_c} \right]_{RMS}^2 k_0^2 L_f [\Delta s_{\parallel}]_f \quad (11)$$

with $N_{\perp,X}$ the component of the refractive index for X-polarization perpendicular to the magnetic field, n_c the cutoff density, defined by $n_c = \bar{n}_e(\omega/\omega_{p,e})^2$ and k_0 the EC beam wave number in vacuum. Figure 3 shows the EC beam broadening at the wave absorption location $s_{\parallel}^{\text{abs}}$, defined by $\Gamma_b = \text{FWHM}[\langle |E| \rangle_{t,\text{fluct}}(s_{\parallel}^{\text{abs}})] / \text{FWHM}[|E|_{\text{quiet}}(s_{\parallel}^{\text{abs}})] - 1$, and the associated power deposition profile broadening plotted against $\log(\lambda_X)$ for all the simulated cases. Also shown is the difference between the coefficient of determination for a Gaussian fit R_G^2 and a Lorentzian fit R_L^2 of the transverse beam section at the absorption location.

To estimate the power deposition profile, a total of 300 rays have been used in C3PO: 50 rays are used in the radial direction to properly reconstruct the Gaussian or Lorentzian beam profile (the error on the beam width is less than 2% between the prescription from COMSOL and the ray discretization), spread in six different directions perpendicular to the beam propagation direction. This discretization may lead to some artifacts in the power deposition profile, as shown in figure 5. In that case, only the base of the power deposition profile is considered, and the sharp, narrow peak is excluded from the Gaussian fit performed to estimate the FWHM of the power deposition profile. It is possible to clearly see the effect of the beam broadening on the width of the base of the power deposition profile (see examples in figure 4). The broadening of the power deposition profile Γ_P is estimated as

Table 1. Analytic equilibrium parameters generated using the method described in [60]. All equilibria are up-down symmetric and share the minor radius $a = 25$ cm, the major radius $R_0 = 88$ cm, the on-axis magnetic field $B_0 = 1.5$ T, the elongation $\kappa = 1.3$, the triangularity $\delta = 0.1$, the pressure gradient $\partial p / \partial \psi_{p,n} = 110^{-4}$ Pa (with $\psi_{p,n} = \rho_{\psi_p}^2$ the normalized poloidal magnetic flux), $T_e = T_i$ and $Z_{\text{eff}} = 1$. The density profile is proportional to $(\rho_{\psi_p})^k$ with $k = 4/3$. The temperature profile is adjusted so that the requested pressure gradient is matched.

| Analytic equilibrium # | AE#1 | AE#2 | AE#3 |
|-----------------------------------|---------------------------------------|---------------------------------------|---------------------------------------|
| On-axis density $n_{e,0}$ | $2.5 \times 10^{-19} \text{ m}^{-3}$ | $2.5 \times 10^{-19} \text{ m}^{-3}$ | $2.5 \times 10^{-19} \text{ m}^{-3}$ |
| Edge density $n_{e,1}$ | $6.25 \times 10^{-18} \text{ m}^{-3}$ | $8.00 \times 10^{-18} \text{ m}^{-3}$ | $6.25 \times 10^{-18} \text{ m}^{-3}$ |
| Edge temperature $T_{e,1}$ | 599 eV | 172 eV | 172 eV |
| Edge Larmor radius $\rho_{L,s,1}$ | 3.0 mm | 1.6 mm | 1.6 mm |

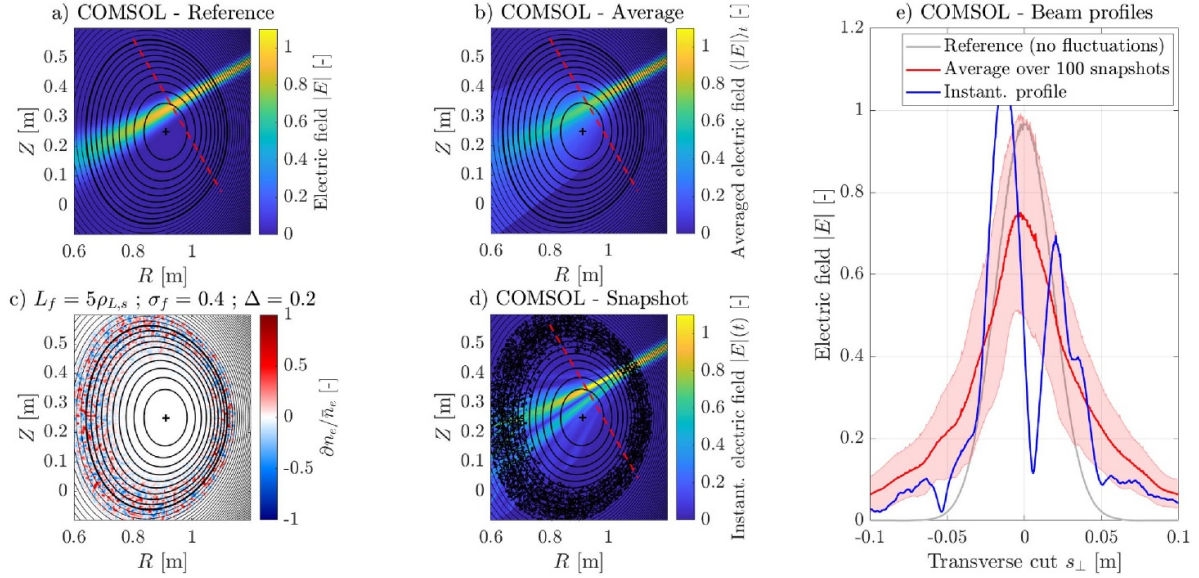


Figure 2. Poloidal view of (a) the EC beam computed with COMSOL in a quiet plasma, (b) the EC beam computed with COMSOL in a turbulent plasma, averaged over 100 fluctuation snapshots, (c) an example of a fluctuation snapshot generated using equation (1) and (d) the associated instantaneous EC beam electric field, computed with COMSOL. The red dashed line indicates the transverse cut along which the electric field is plotted in (e).

Table 2. Scanned fluctuation parameters for different analytic equilibria, using 1D Gaussian envelope $F_{\Delta} = \exp(-(\rho_{\psi_p} - 1)^2 / \Delta^2)$ for the fluctuation model.

| Scan # | Equilibrium | σ_f | Δ | L_f |
|--------|-------------|------------|------------------|-------------------|
| S#1.1 | AE#1 | 0.4 | 0.10 | 1–12 $\rho_{L,s}$ |
| S#1.2 | AE#1 | 0.2–0.8 | 0.02, 0.10 | 5 $\rho_{L,s}$ |
| S#2.1 | AE#2 | 0.4 | 0.10, 0.15, 0.20 | 1–10 $\rho_{L,s}$ |
| S#3.1 | AE#3 | 0.4 | 0.10, 0.20 | 1–10 $\rho_{L,s}$ |

the ratio of the FWHM of the fit for a case with fluctuations to the quiet case, minus 1. This fitting process is illustrated in figure 5. The obtained broadening Γ_p is thus a convenient parameter to qualitatively assess the relative impact of the beam broadening on the power deposition profile. It is important to note that the discretization artifact completely disappears when using 50×20 rays instead of 50×6 , at the cost of a substantially increased numerical expense (roughly by a factor 4).

Three different beam broadening regimes can be described from these results. For $\log(\lambda_X) \ll 0$, the beam bulk is not very affected, and the transverse beam profile remains a nearly unmodified Gaussian, with a non-zero background electric field resulting from the beam scattering. This mode corresponds to the so-called superdiffusive regime described in [20]. On the other hand, for $\log(\lambda_X) \geq 0$, the beam clearly broadens and its transverse profile is either a broadened Gaussian or Lorentzian, as both Gaussian and Lorentzian fits quite well the transverse beam profile, with a small difference between the coefficients of determination of the respective fits. This corresponds to the diffusive regime described in [20]. An intermediate regime can also be identified for $\log(\lambda_X) \leq 0$, where the beam FWHM does not significantly increase, but the beam's transverse profile is distorted by scattering off the density blobs and becomes closer to a Lorentzian than a Gaussian, with non-negligible wings rising on the side of the bulk beam. This intermediate regime represents a smooth transition between the superdiffusive and the diffusive regime, with the sides of the beam profile being affected before the bulk. Such

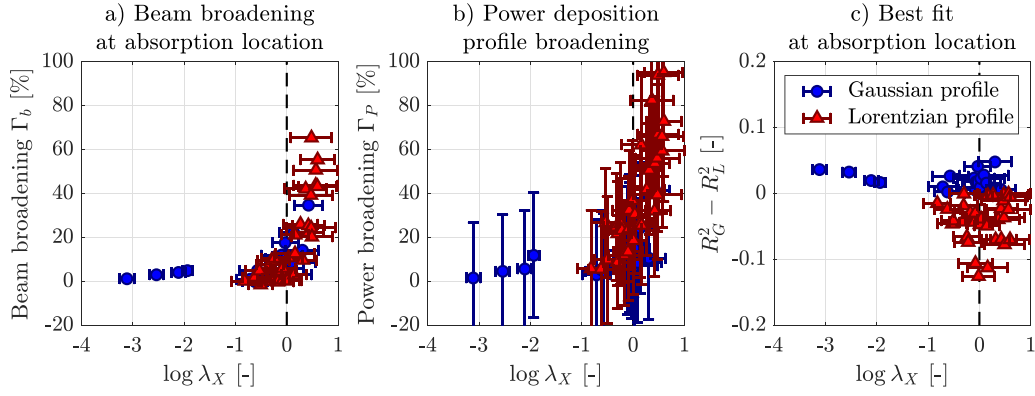


Figure 3. Broadening of the beam FWHM at the absorption location (a), broadening of the base of the power deposition profile (b) and difference in the coefficient of determination between a Gaussian and a Lorentzian fit of the transverse beam electric field profile from COMSOL simulations (c) for the scans summarized in table 2, plotted against $\log(\lambda_X)$ (see equation (11)). The coefficient of determination of the fit is used to determine whether the shape of the beam at the absorption location is Gaussian or Lorentzian. Error bars on λ_X come from the variation of the profiles within the turbulent layer. Error bars on the power deposition broadening come from the 95% confidence interval of the Gaussian fits. All cases are ECRH cases.

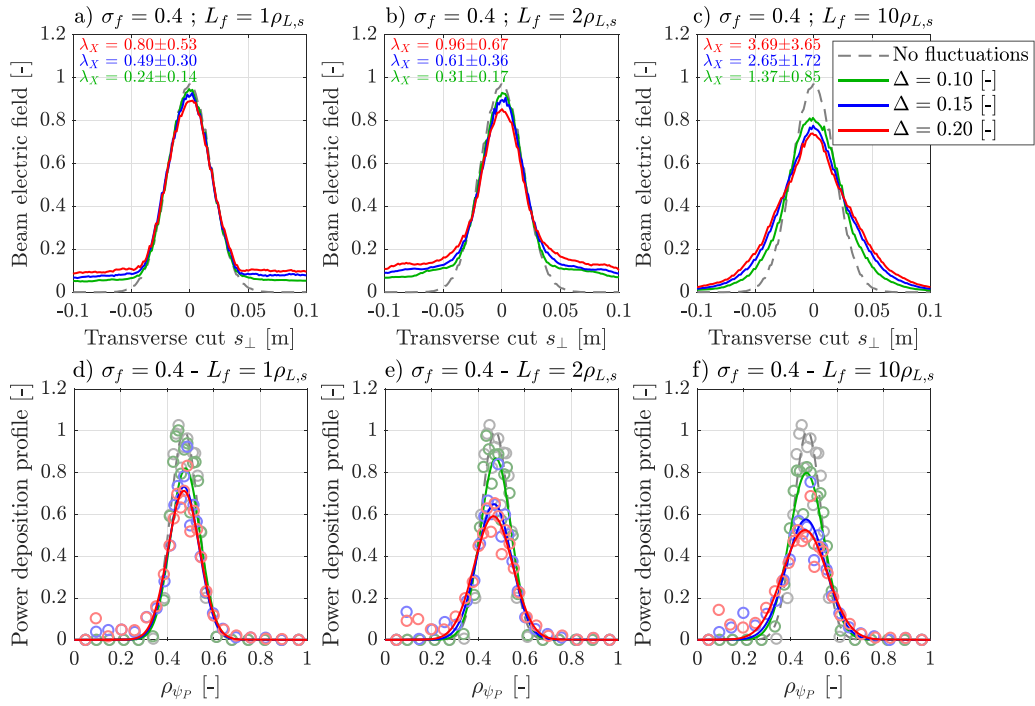


Figure 4. Transverse cut of the beam electric field averaged over 100 fluctuation snapshots, taken at the wave absorption location in equilibrium AE#2 (see table 1), computed by COMSOL and illustrating the superdiffusive regime (a), the intermediate regime (b) and the diffusive regime (c) of EC beam broadening. Associated Gaussian fits of the base of the power deposition profile (sharp, narrow peak has been removed) are shown in panels (d), (e) and (f) respectively. All cases are ECRH cases.

Lorentzian beam shapes have already been observed in other full-wave studies [22]. These three regimes are illustrated in figure 4, which shows examples of transverse beam profiles for different fluctuation cases. As expected, the power deposition profile broadening increases with the beam broadening. However, a Lorentzian-shaped beam can also lead to power deposition profile broadening while having a beam FWHM close to the quiet case.

The worst case scenario, corresponding to a large power deposition profile broadening, is mainly the diffusive regime,

although the intermediate regime can lead to a non-negligible power deposition profile broadening too (see figure 4). At a given EC beam frequency, the beam broadening is increased for high relative density fluctuation RMS $[\delta n_e / \bar{n}_e]_{RMS}$ and high level of absolute background density \bar{n}_e , as well as for a large turbulent layer width $[\Delta s_{\parallel}]_f$. To maximize the beam broadening, the fluctuation size L_f should be close to the order of the beam wavelength λ_0 . If $L_f \ll \lambda_0$, the beam broadening is superdiffusive and the bulk of the beam is not affected. On the other hand, for very large fluctuation structures, typically $L_f \gg$

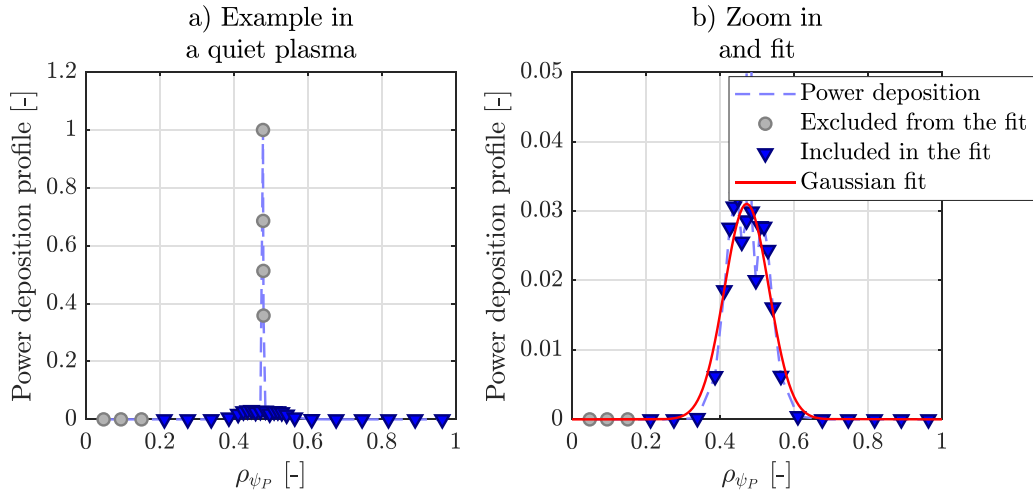


Figure 5. Example of fitting of the base of the power deposition profile, for a quiet plasma, using equilibrium AE#2 (see table 1). The beam is launched in ECRH configuration.

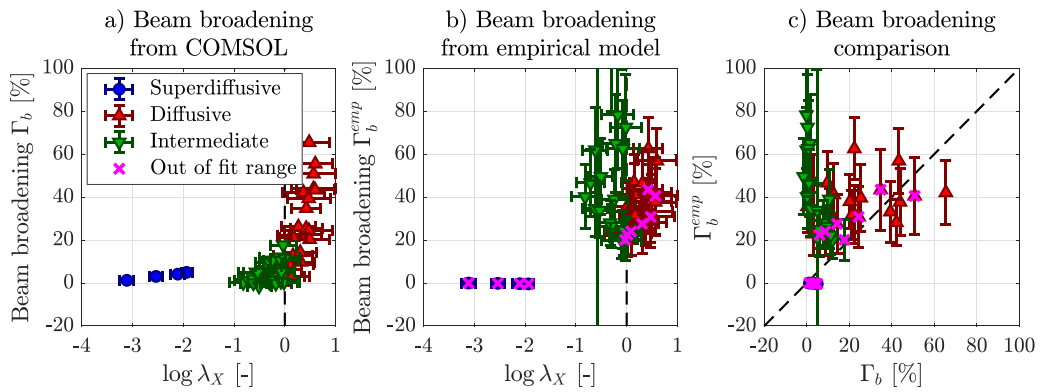


Figure 6. Comparison between the beam broadening estimated with COMSOL Γ_b and with the semi-empirical model Γ_b^{emp} developed in [23]. The magenta crosses represent points for which at least one parameter is out of the fit range.

w_0 , the density fluctuations only impact the beam refraction, leading to almost no impact on beam width (see section 5.2 for an example). The present numerical study also highlights the fact that, in TCV, the X2 82.7 GHz beam broadening regime is most likely the intermediate beam broadening regime. The dependencies of the beam broadening on the different plasma and fluctuation parameters have been extensively studied in [23], using 2D full-wave simulations, yielding a semi-empirical formula to quickly estimate the FWHM broadening of the beam. This study focuses on parameters relevant for machines larger than TCV, such as DIII-D or ITER, and thus mainly on the diffusive broadening regime. It does not take into account the potential change in the shape of the beam, which can lead to a broader power deposition profile while the beam FWHM does not change much with respect to the quiet plasma case. As shown in figure 6, the semi-empirical model gives good estimates of beam broadening for the diffusive regime cases, but overestimates drastically the broadening for the intermediate regime cases, which are close to the limits of the fit parameters (and so to the validity domain

of the fit). The model values have been estimated using linear interpolation of data in table A1 of [23]. Analytical formulas derived from wave-kinetic theory are also available to estimate the broadened width of O-mode [12] and X-mode [13] microwave beams propagating in 2D, but they are limited to Gaussian beam profiles in the low fluctuation level limit.

5. Experimental study: can beam scattering alone explain the discrepancy between observations and simulations?

5.1. Experimental setup

Two different experimental ECCD scenarios are proposed to study the impact of turbulence on beam scattering in TCV. Scenario A, illustrated in figure 7(a), minimizes the impact of beam broadening on the power deposition profile, as the power deposition is spread within a given flux surface. On the

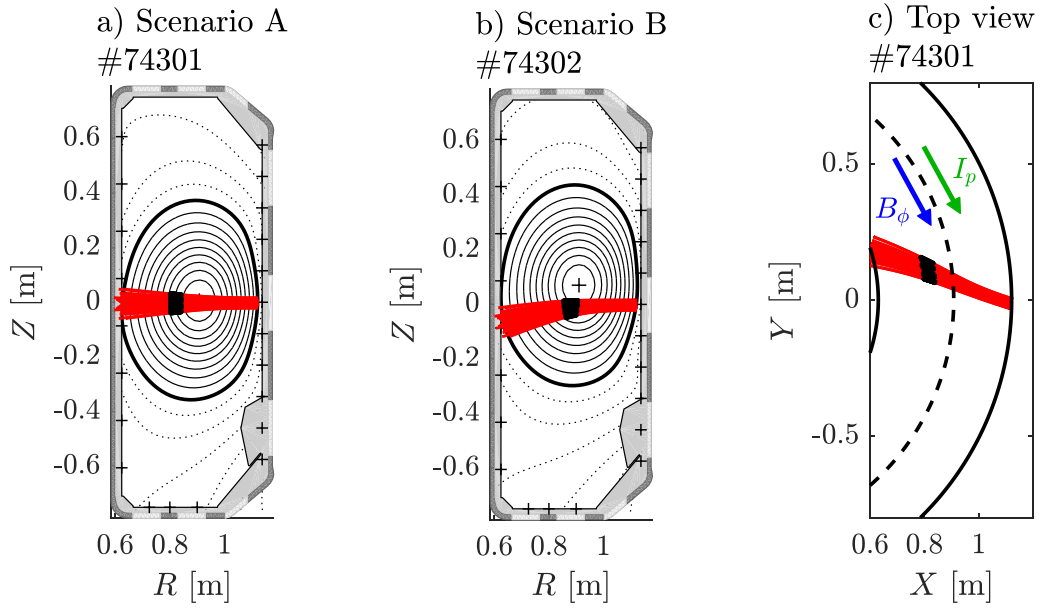


Figure 7. Results of C3PO ray tracing for the three different scenarios developed at TCV: a configuration minimizing the impact of density fluctuations on EC power deposition profile broadening (a) and a configuration maximizing this impact (b). Top view of scenario A (c), showing the plasma current I_p and the toroidal magnetic field B_ϕ directions. The configuration is co-ECCD.

other hand, scenario B, illustrated in figure 7(b), maximizes this impact as the power is spread perpendicularly to the flux surfaces. In both scenarios, the 82.7 GHz X-polarized EC wave is steadily injected in the co-current direction, from 0.7 s to 2.5 s (the wave is absorbed at the second harmonic location in the plasma). The equilibrium is averaged between 1.25 s and 1.55 s. At these times, the current induced by the wave absorption has had the time to diffuse completely. The profiles and time traces of the main plasma quantities are shown in figure 8 for the main TCV shots of the present study, namely TCV shots #74301 and #74302, as well as TCV shot #77460 which is a replica of #74301 used as a reference for SPR measurements.

As mentioned in section 2, information about the density fluctuation profile is obtained from SPR measurements. However, this experimental characterization is limited to $\rho_{\psi_p} \leq 0.95$; therefore, the profile is extrapolated using a Lorentzian fit until the LCFS at $\rho_{\psi_p} = 1$ and a constant value is assumed in the SOL, the free parameter being the RMS value at the LCFS $[\delta n_e/\bar{n}_e]_{\text{RMS},1}$ and measurements fixing the background fluctuation level $[\delta n_e/\bar{n}_e]_{\text{RMS},0}$. Two values of edge density fluctuation level have been studied, $[\delta n_e/\bar{n}_e]_{\text{RMS},1} = 60\%$ and $[\delta n_e/\bar{n}_e]_{\text{RMS},1} = 80\%$, the first one corresponding to what is expected in TCV [36] and the second to a more extreme case. The typical fluctuation correlation length is set to $L_f = 10\rho_{L,s}$. These profiles are illustrated in figure 9 for TCV shot #77460. As shown in figure 10, the expected beam broadening regime for these two values, and for both scenarios A and B, ranges between the superdiffusive and intermediate regimes, as described in section 4. A summary of the TCV shots used for this study is given in table 3.

5.2. Methodology for the ECCD cases and justification

As mentioned in section 3.1, the full-wave COMSOL simulations are limited to 2D configurations only, which makes it challenging to properly model the effect of edge density fluctuations on beam broadening in ECCD configurations. This means that the studied ECCD configuration must be constrained to cases in which the beam propagates in a plane. This is the case for the scenarios A and B (at least before the beam absorption, see figure 7), respectively minimizing and maximizing the effect of the beam broadening on the power deposition profile, for which a toroidal section can be considered instead of a poloidal section. The fluctuation model detailed in section 2 assumes field-aligned structures that are toroidally homogeneous. This is illustrated in figures 11(a) and (b).

A test case is used to assess the validity of using a toroidal section instead of a poloidal one to study the impact of turbulence on beam broadening. As shown in figure 11, an X-polarized beam in ECRH mode is propagated along the plasma equatorial midplane, and its broadening through an edge-localized fluctuation layer is studied in three different 2D configurations: a standard poloidal section (figure 11(a)), the corresponding toroidal section (figure 11(b)) and a modified toroidal section, using an artificial fluctuation pattern imitating the poloidal structure (characteristic eddy size) in the toroidal direction (figure 11(c)). It can be seen in figure 11(d) that, on average, the beam FWHM does not change much between the different cases. However, for the poloidal and modified toroidal cases, the beam profile is distorted and evolves from a Gaussian to a Lorentzian profile along the propagation direction. This is illustrated in figure 11(e), which shows the beam electric field transverse to the beam propagation at the wave

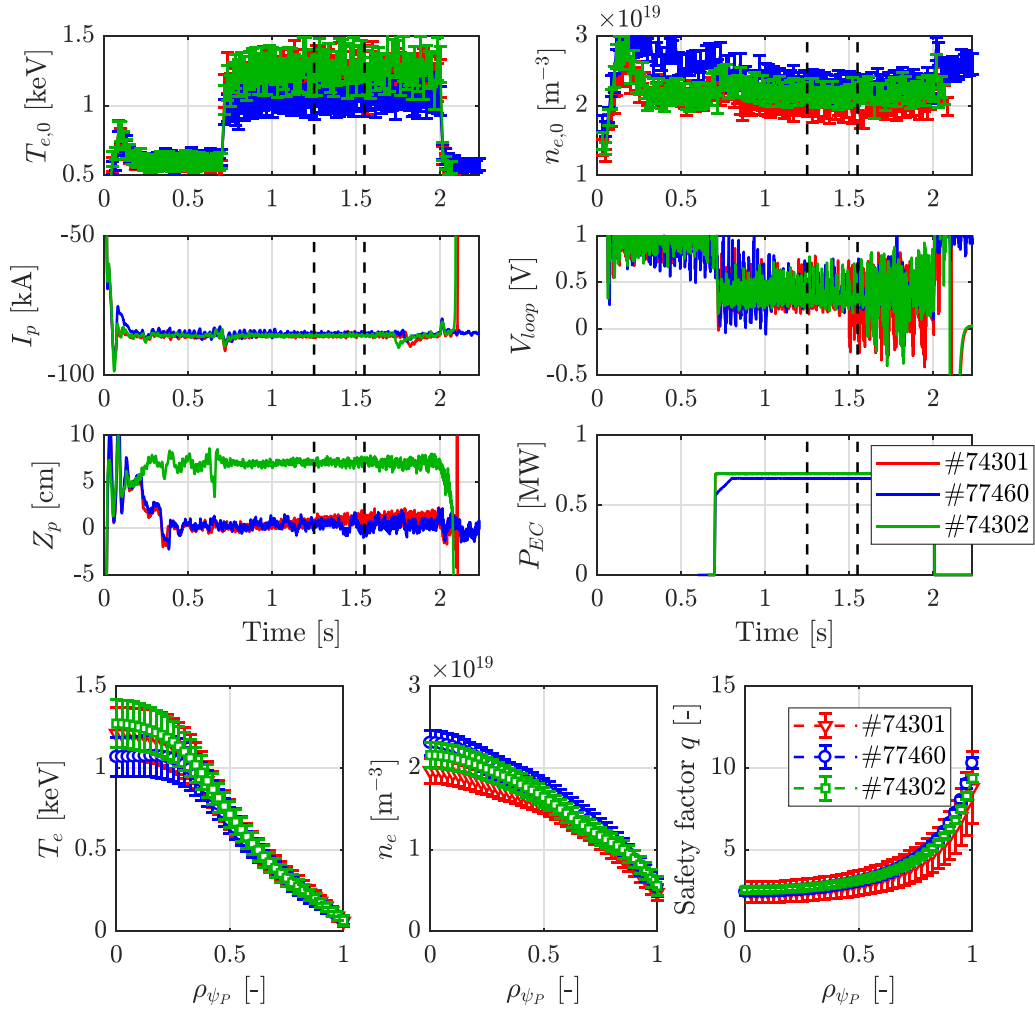


Figure 8. Time traces of central electron temperature and density, plasma current, loop voltage, plasma vertical position and EC injected power, as well as profiles of electron temperature and density and safety factor for TCV shots #74301 and #77460, corresponding to scenario A, and TCV shot #74302 corresponding to scenario B. The black dashed lines on time traces represent the time interval over which profiles are averaged.

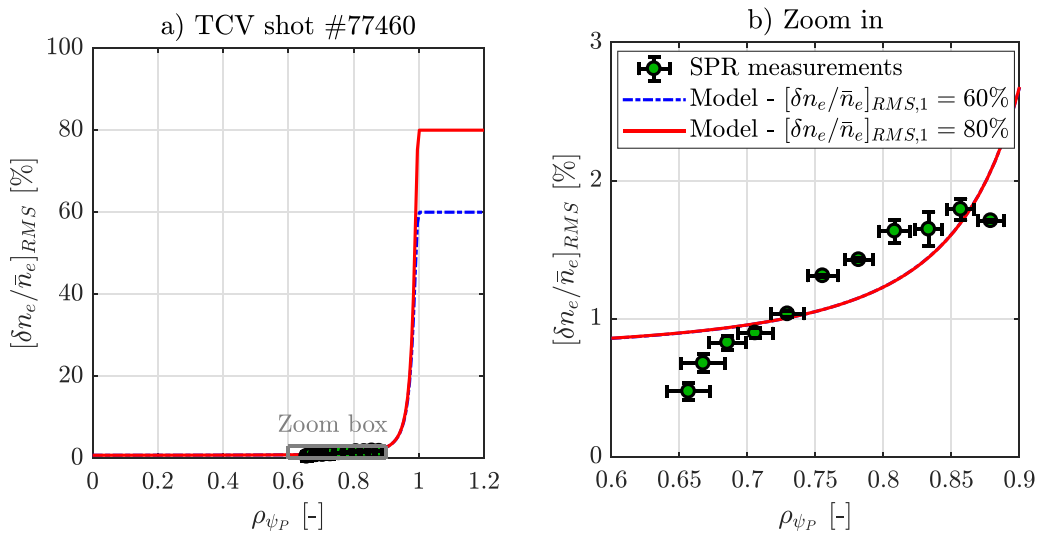


Figure 9. Short Pulse Reflectometry (SPR) data for TCV shot #77460 and associated Lorentzian models for two different values of density fluctuation RMS at the LCFS. The density fluctuation RMS is assumed constant in the SOL. The error bars on the experimental data are statistical error bars from time averaging.

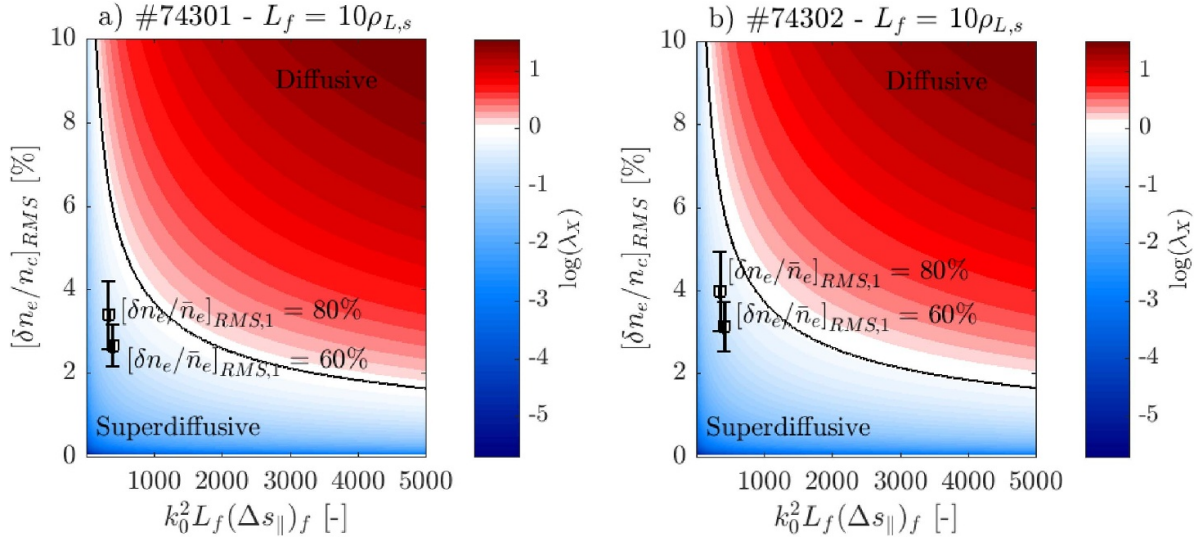


Figure 10. Expected beam broadening regime for scenario A (a) and scenario B (b), for the tested fluctuation parameters. The parameter λ_x is calculated using equation (11).

Table 3. List of TCV shots used in the present study.

| Shot # | Scenario | Diagnostics | EC beam ^a | | Parameters | |
|--------|----------|-------------|--|---|-----------------------------------|------------|
| | | | θ_0^{abs} (°) ^b | $\rho_{\psi_p}^{\text{abs}}$ (-) ^c | Z_{eff} (-) ^d | Z_p (cm) |
| 74 301 | A | HXRS | $-64.2 \pm 1.7^\circ$ | 0.38 | 1.10 | 0.6 |
| 77 460 | A | SPR | $-63.1 \pm 1.5^\circ$ | 0.36 | 1.10 | 0.4 |
| 77 458 | A | SPR | $89.7 \pm 0.1^\circ$ | 0.41 | 1.10 | 0.8 |
| 74 302 | B | HXRS | $-63.7 \pm 1.3^\circ$ | 0.31 | 1.35 | 7.1 |
| 77 456 | B | SPR | $-89.0 \pm 0.1^\circ$ | 0.23 | 1.35 | 7.0 |

^a EC power is 725 kW for shots #74301 and #74302, and 691 kW in all other cases;

^b θ_0^{abs} is the angle between the wave vector and the magnetic field at absorption location (negative for co-ECCD);

^c $\rho_{\psi_p}^{\text{abs}}$ is the absorption location in normalized poloidal flux coordinates;

^d From LUKE estimations, matching I_p with experiments in ECRH.

absorption location. Here, it is clear that the standard toroidal case does not reproduce the broadening observed in the standard poloidal case, while the modified toroidal case matches the poloidal one well.

Two main consequences arise from this test. First, the beam broadening in the presence of field-aligned structures, assuming a poloidal correlation length of the same order (or smaller) as the beam width, is anisotropic, and the beam mainly broadens in the poloidal direction. The second consequence is that, to model the beam propagation in a turbulent plasma for a 2D ECCD configuration, it is preferable to use the modified toroidal fluctuation pattern, which reproduces the poloidal beam broadening, as the coupling between COMSOL and LUKE assumes an EC beam with an azimuthally symmetric transverse cross-section. This limit maximizes the overall broadening with respect to a case with a realistic 3D fluctuation pattern. For the present study, we are interested in a worst case scenario to be compared with experimental data, but if one wants to improve the prediction capabilities of the numerical tools, the use of a 3D wave propagation solver is required, at least to treat ECCD configurations.

5.3. COMSOL-LUKE simulations of experimental cases

COMSOL-LUKE simulations have been performed for TCV shots, using 50×20 rays for the coupling via the custom beam width in C3PO. LUKE simulations require an estimation of the effective charge Z_{eff} . For the ECCD cases (TCV shots #74301 and #74302 for scenarios A and B respectively), the effective charge is obtained, assuming a constant profile, by matching the plasma current from LUKE simulations I_p^{LUKE} in pure ECRH cases (TCV shots #77458 and #77456 for scenario A and B respectively) with the experimental plasma current I_p from which the bootstrap current I_{BS} has been removed (the bootstrap current is not simulated in LUKE), so that $I_p^{\text{LUKE}} = I_p - I_{BS}$. Indeed, for pure ECRH cases, the current driven by the EC waves is negligible and the effective charge can be used as a free parameter to match the experimental current. This gives the Z_{eff} values indicated in table 3. LUKE simulations have been performed in time-asymptotic mode, which is the most relevant mode for the present experiments as the typical characteristic time for the wave-induced electric field diffusion is of the order of 0.01 to 0.1 s in limited L-mode TCV plasmas [7, 8].

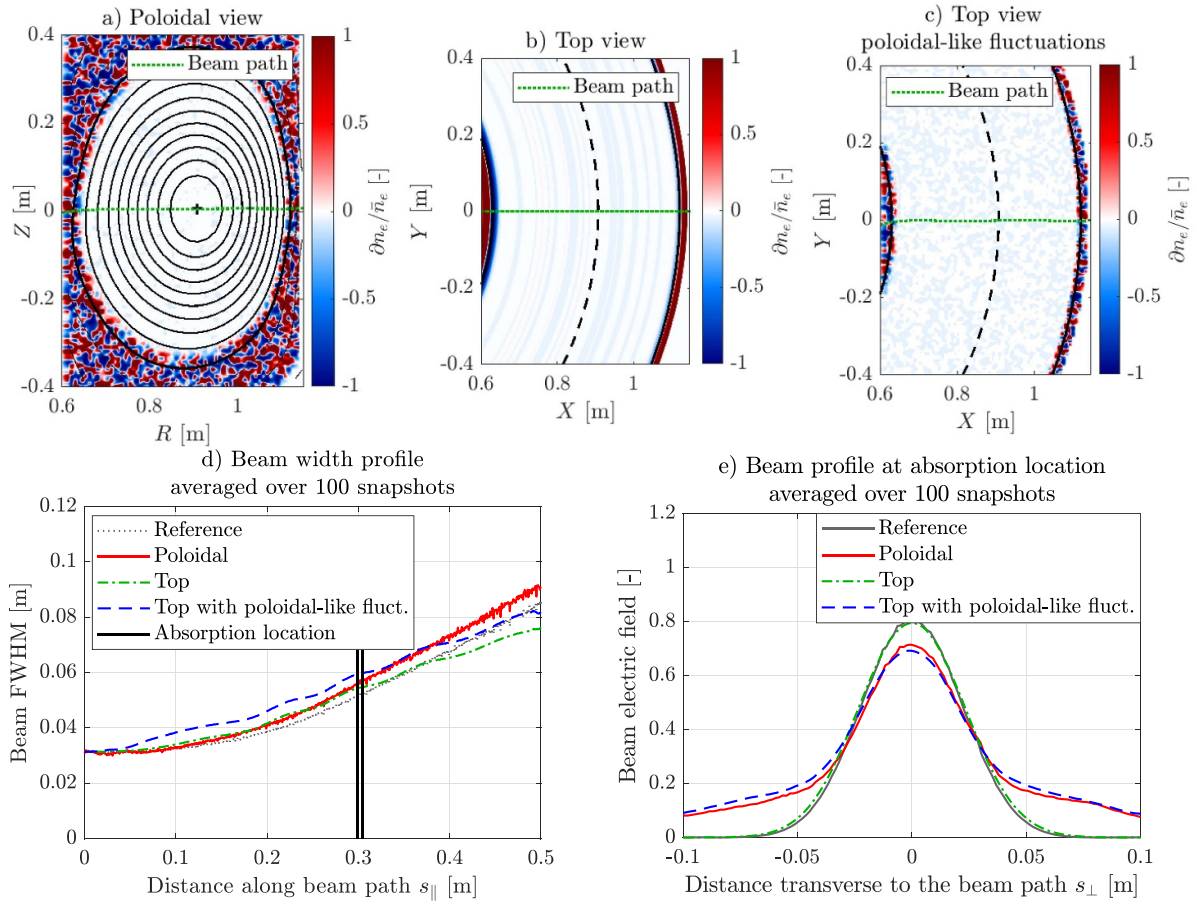


Figure 11. Results of 2D COMSOL simulations showing the beam FWHM along the beam path (*d*) and the associated beam transverse section at the absorption location (*e*) for configurations (*a*) (poloidal section), (*b*) (toroidal section) and (*c*) (toroidal section, but using poloidal-like density fluctuations).

Results from COMSOL simulations, showing the beam width and beam transverse section at the absorption location for the two scenarios, are given in figure 12. The beam FWHM increases slightly, but does not change much with increasing RMS of the density fluctuations. However, the beam profile is distorted from a Gaussian to a Lorentzian shape. These features are characteristic of the intermediate beam broadening regime, described in section 4, matching the expectations obtained using equation (11) (see figure 10). Finally, one can notice that the beam scattering leads to an asymmetric beam profile, and this asymmetry increases with the density fluctuation RMS. The average beam refraction is negligible. In the worst case, at the absorption location, the beam is shifted by 1 mm with respect to the reference case. In both scenarios, a comparable beam broadening is observed for the different fluctuation patterns that have been tested, in spite of the fact that the beam travels over a slightly longer distance before being absorbed in scenario A. The resulting absorbed EC power profile is shown in figure 13. It can be clearly seen that, for scenario A, the impact of edge density fluctuations on the power deposition profile is almost negligible, while the power deposition profile significantly broadens for scenario B, even though the beam broadening is similar in both

cases. This confirms that the impact of beam broadening on the actual power deposition profile is also dependent on the beam launching configuration, and that scenario A minimizes this impact.

Results from COMSOL-LUKE simulations are compared to experimental HXRS data in figure 14 for scenario A (TCV shot #74301) and in figure 15 for scenario B (TCV shot #74302). The first important observation is that the impact of density fluctuations on the simulated HXR count rate is almost negligible for scenario A. On the other hand, the impact of density fluctuations is clearly visible in scenario B, where the increase of the density fluctuation RMS induces a flattening of the HXR distribution. However, in both cases, the measured HXR count rate is around one order of magnitude lower than what is estimated using time-asymptotic COMSOL-LUKE simulations.

The calculated plasma current is overestimated by $\sim 158\%$ in scenario A, and by $\sim 97\%$ in scenario B when considering $[\delta n_e / \bar{n}_e]_{\text{RMS},1} = 60\%$ and by $\sim 67\%$ when considering $[\delta n_e / \bar{n}_e]_{\text{RMS},1} = 80\%$. For the reference case for scenario B, without considering fluctuations, the current is overestimated by $\sim 186\%$. The high electric field, coupled to the EC wave absorption, can accelerate some electrons up to the

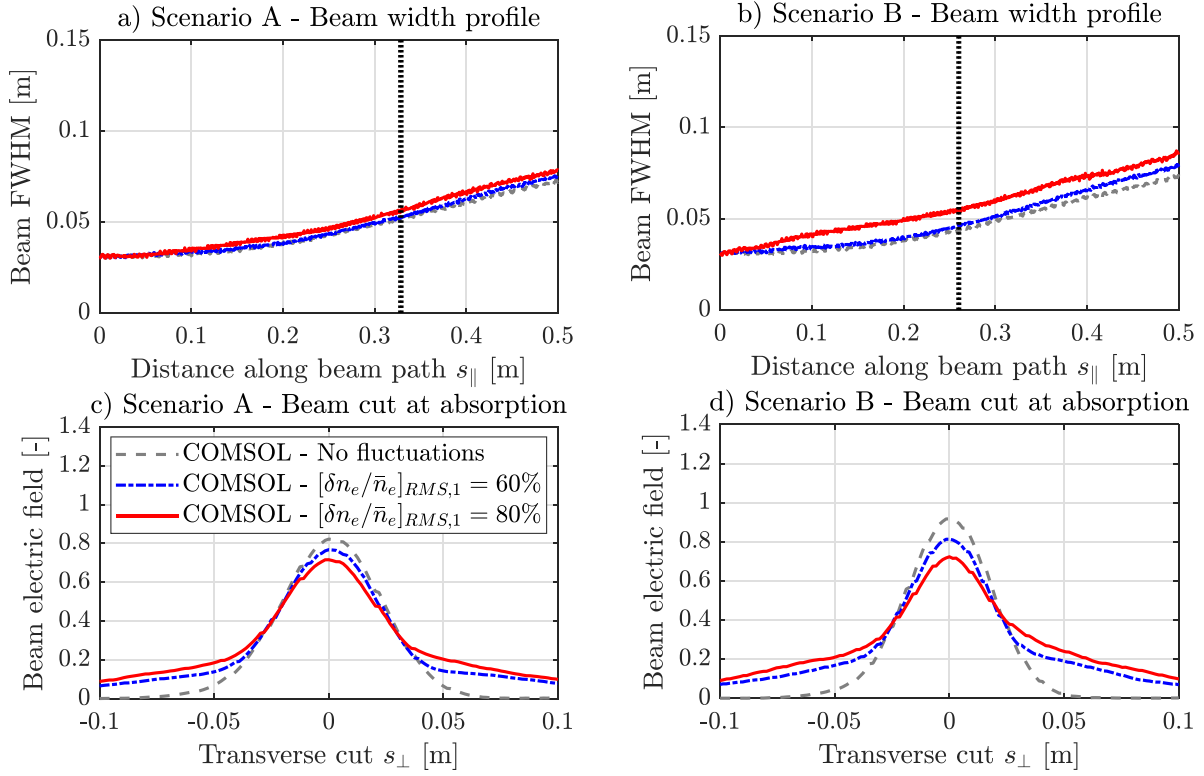


Figure 12. Beam width profile for scenario A (TCV shot #74301) (a) and scenario B (TCV shot #74302) (b), as well as beam transverse profile at beam absorption location for scenario A (c) and scenario B (d), computed using COMSOL and poloidal-like top fluctuations, as shown in figure 11(c). Black dotted lines show the absorption location along the beam path.

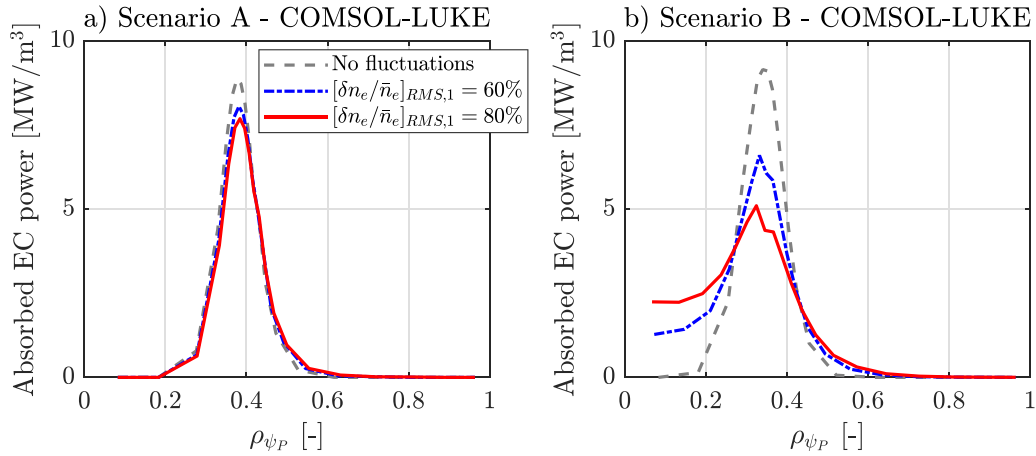


Figure 13. Power deposition calculation performed using COMSOL-LUKE in time-asymptotic mode for scenario A (TCV shot #74301) (a) and scenario B (TCV shot #74302) (b).

runaway regime. A few runaway electrons can then carry a significant portion of the total plasma current (from 12% to 34% in these time-asymptotic simulations). The effect of density fluctuations tends to reduce the calculated driven current, as well as to reduce the current fraction carried by runaway electrons, which means that the simulation results get closer to the experimental observations. However, in the tested configurations, this effect is not sufficient to bridge the gap between simulations and experiments.

In practice, the electric field in the simulations is above the critical electric field for runaway electron generation E_{crit} , given by [61]

$$E_{crit} = \frac{e^3 n_e \ln \Lambda}{4\pi \epsilon_0^2 m_e c^2} \quad (12)$$

where $\ln \Lambda$ is the Coulomb logarithm for electron-electron collisions. It is worth noticing that, experimentally, there is no evidence of a significant presence of runaway electrons. In

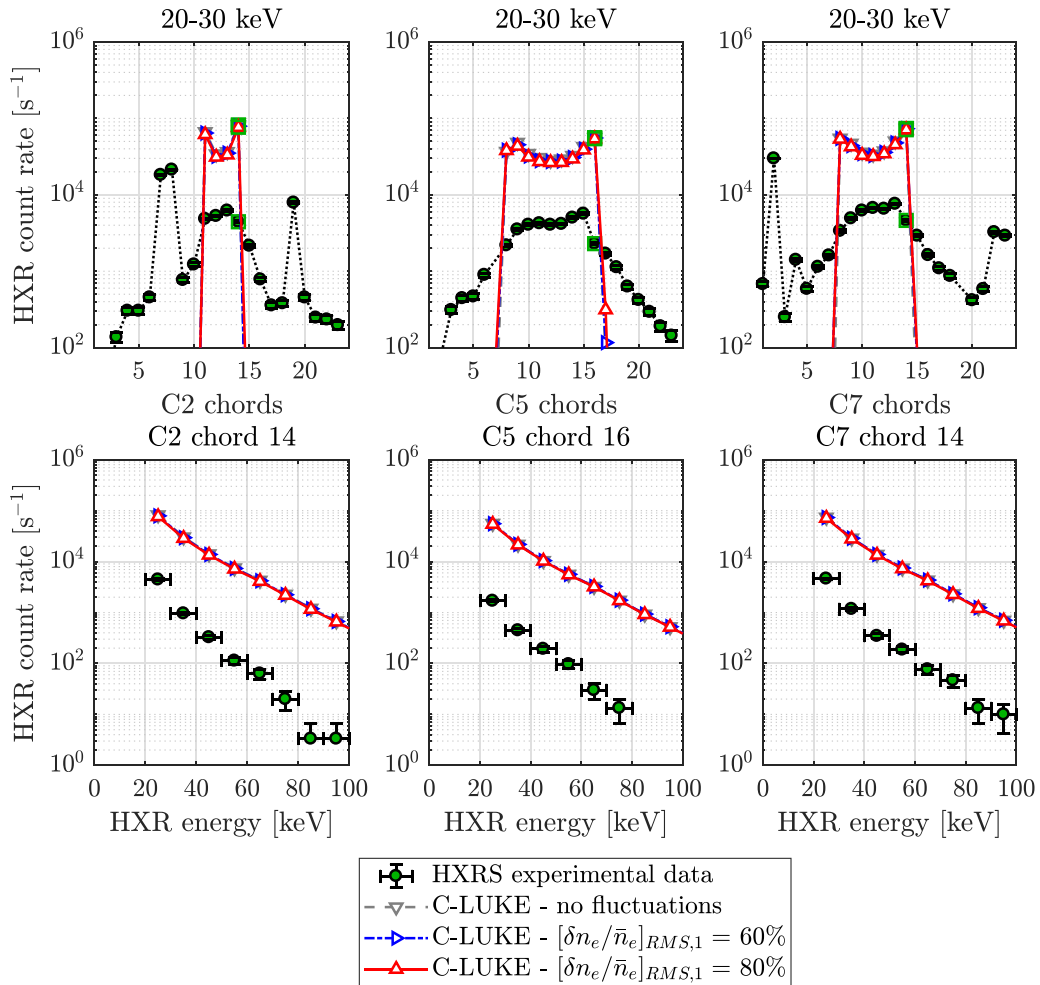


Figure 14. Hard x-ray (HXR) count rate measured by the HXRS and estimated from COMSOL-LUKE simulations (C-LUKE), using both the time-asymptotic mode, for different density fluctuation conditions, for TCV shot #74301 (scenario (A)). The green squares on the top panels indicate the selected chords for which the HXR spectrum is plotted in the bottom panels. Note that the three types of symbols for each color (gray, blue and red) are almost exactly superimposed and thus not all visible.

the time-asymptotic simulations, no radial transport of electrons has been added, and so, the confinement time of runaway electrons in these simulations corresponds to an overestimated, ideal confinement time. Moreover, recent studies performed in TCV conclude that ECRH/CD tend to degrade the confinement of runaway electrons, leading to their expulsion from the plasma [62]. Therefore, additional LUKE simulations have been performed, removing part of the runaway electron domain in velocity space, corresponding to momentum $p \geq p_{\text{crit}}$, with $p_{\text{crit}} = m_e c (E_{\parallel} / E_{\text{crit}} - 1)^{-1/2}$ [61]. A comparison between synthetic and experimental HXRS data is shown for scenario B in figure 16. These simulations aim at verifying the impact of density fluctuations on the HXR generation, without the influence of this artificial runaway electron population. However, by completely removing the runaway electron domain, part of the suprathermal electrons are also removed, thus artificially reducing the synthetic HXR count rate at higher energies. Therefore, a compromise is made for these simulations, minimizing the contribution of runaway electrons, which gives a lower bound to the synthetic HXR

count rate in the time-asymptotic mode. As shown in table 4 and figure 16, even in this configuration, the effect of density fluctuations on the EC power deposition profile is not sufficient to explain the discrepancy between LUKE and the experimental HXRS data.

The density-fluctuation-induced flattening of the HXR distribution is still not sufficient to explain the discrepancy between the measurement and the simulations, even though the studied beam broadening has been maximized (highest realistic level of density fluctuation RMS, isotropic beam broadening). It means that another mechanism plays a dominant role in explaining the broadening of the suprathermal electron distribution observed in these TCV configurations. The proposed mechanism is a wave-enhanced radial transport of the fast electrons, which has been first inferred in [7] where an ad-hoc radial transport proportional to the phase-space-localized EC wave diffusion was used to match experimental data. This electron transport has then been associated to an increase of turbulent transport with the EC wave power in [8]. This does not mean

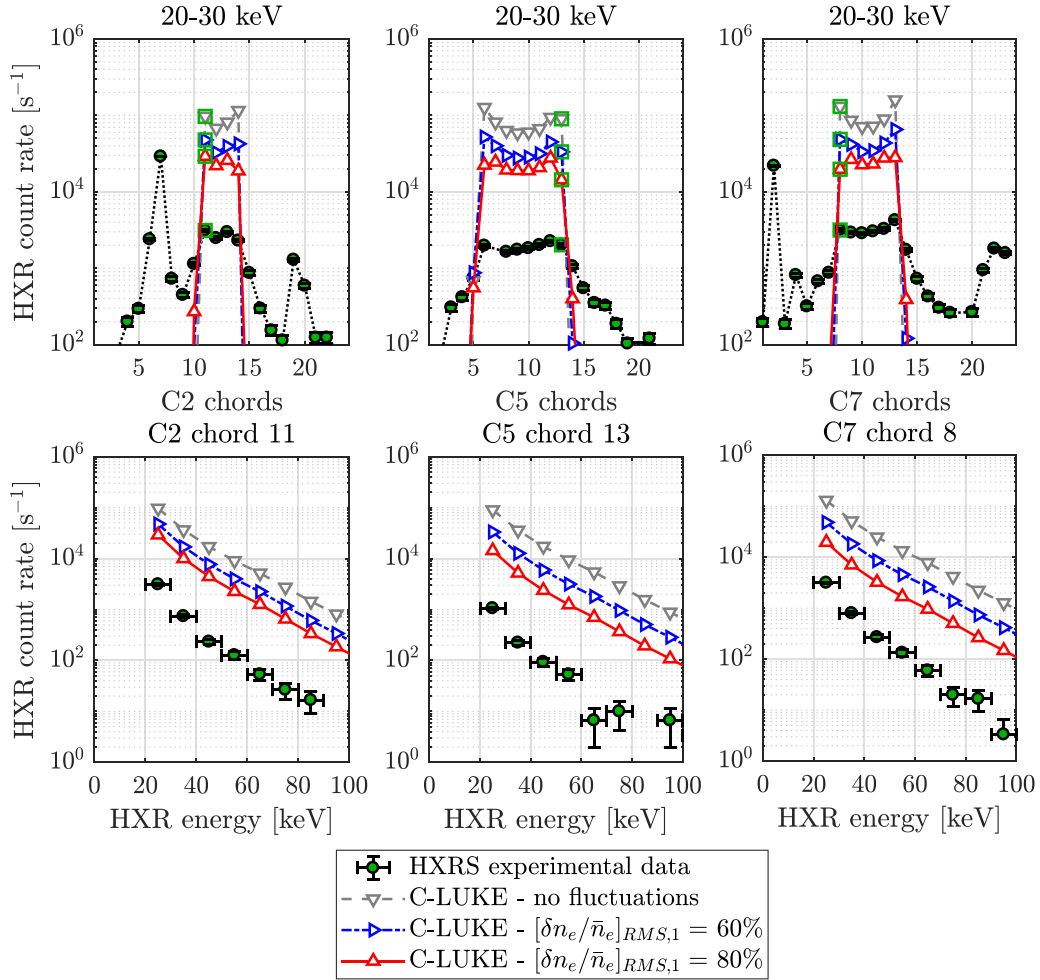


Figure 15. Hard x-ray (HXR) count rate measured by the HXRS and estimated from COMSOL-LUKE simulations (C-LUKE), using both the time-asymptotic mode, for different density fluctuation conditions, for TCV shot #74302 (scenario (B)). The green squares on the top panels indicate the selected chords for which the HXR spectrum is plotted in the bottom panels.

that, for other machine conditions, the EC beam broadening cannot be the dominant mechanism. In particular, the effect of density fluctuations is expected to have an important impact in the case of long beam path before wave absorption far in the diffusive beam broadening regime (e.g. for

high density fluctuation RMS with respect to the EC cutoff density, or for turbulent layer width much larger than the EC wavelength), as can happen in bigger machines like ASDEX-Upgrade [20] and potentially in future large devices like ITER [17, 20].

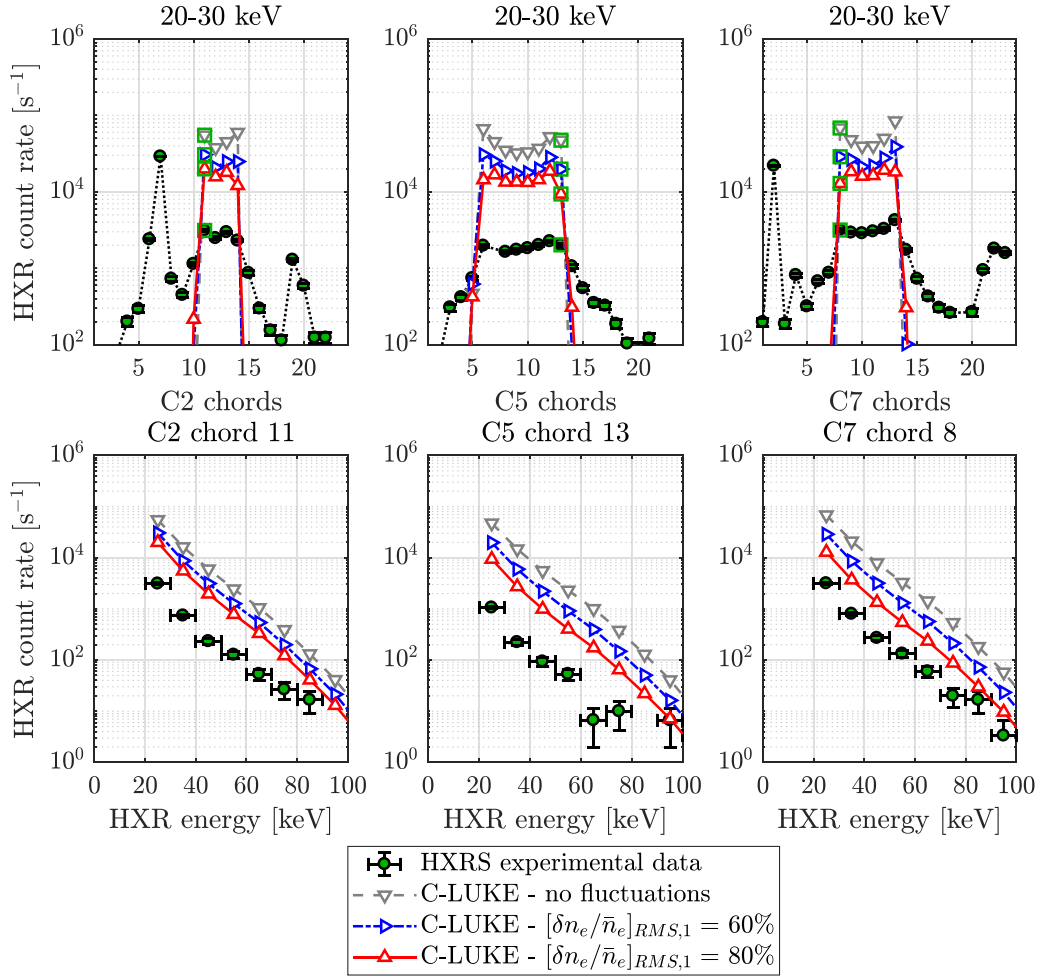


Figure 16. Hard X-Ray (HXR) count rate measured by the HXRS and estimated from COMSOL-LUKE simulations (C-LUKE), using the time-asymptotic mode, for different density fluctuation conditions, for TCV shot #74302 (scenario (B)). The green squares on the top panels indicate the selected chords for which the HXR spectrum is plotted in the bottom panels. Runaway electron domain has been partly removed from velocity space, corresponding to $p \geq 15 p_{Te}$ ($p_{crit} \simeq 11 p_{Te}$) at the EC wave absorption location, with p_{Te} the thermal momentum.

Table 4. Current calculated by LUKE in time-asymptotic mode. I_{RE} stands for the runaway electron current. The target plasma current is 78 kA for both scenario A and scenario B.

| Scenario | $[\delta n_e / \bar{n}_e]_{RMS,1}$ | I_p^{LUKE} (kA) | I_{RE}^{LUKE} (kA) |
|----------------|------------------------------------|-------------------|----------------------|
| A | — | 204 | 54 |
| A | 60% | 200 | 54 |
| A | 80% | 196 | 52 |
| B | — | 223 | 76 |
| B | 60% | 154 | 30 |
| B | 80% | 130 | 15 |
| B ^a | — | 149 | 7 |
| B ^a | 60% | 126 | 4 |
| B ^a | 80% | 117 | 2 |

^a Runaway electron domain partly removed from velocity space, corresponding to $p \geq 15 p_{Te}$ ($p_{crit} \simeq 11 p_{Te}$) at EC wave absorption location, with p_{Te} the thermal momentum;

6. Conclusions

The impact of EC beam broadening, caused by the beam scattering off the turbulent density structures, on the

power deposition profile has been numerically and experimentally studied in TCV. Contrary to previous experimental studies performed in TCV [28, 29], the present study focuses on an EC beam launched from the LFS,

which is fully absorbed at the second harmonic resonant location.

First, a full-wave numerical study performed in a TCV-like configuration allows the identification of different beam broadening regimes, recovering results from previous numerical studies [20]. It is shown that, in TCV, the most probable beam broadening regime is an intermediate regime between diffusive and superdiffusive regimes, in which the beam is distorted from a Gaussian into a Lorentzian shape, but the beam FWHM is not increased significantly with respect to the quiet plasma case. The numerical tools have been adapted to treat the absorption of such Lorentzian beams, coupling the full-wave COMSOL model to the drift-kinetic bounce-averaged Fokker–Planck solver LUKE.

Experimental scenarios have been developed in TCV to investigate the possibility that beam broadening could explain the unresolved discrepancy between the measured hard x-rays, emitted from suprathermal electron Bremsstrahlung, and the synthetic diagnostic results from LUKE/R5-X2 [3, 4]. Relative density fluctuations are measured within the plasma edge by short pulse reflectometry, and profiles are extrapolated based on previous reciprocating Langmuir probe measurements [36]. Multiple conclusions can be drawn from the comparison between experimental results and worst-case-scenario simulations. First, the launching configuration plays a very important role in the impact of the beam broadening on the power deposition profile broadening: this impact is minimized for a beam propagating along the plasma equatorial midplane. In any event, in all tested TCV configurations, the impact of the beam broadening is not sufficient to explain the aforementioned discrepancy. It is possible that, for such configurations, the enhanced turbulent transport by the EC wave absorption also plays a significant role in the flattening of the hard x-ray distribution [7, 8]. Both effects do not exclude each other, and it is possible that, in other configurations (e.g. far in the diffusive beam broadening regime), beam broadening could indeed become the dominant mechanism.

To better assess the beam broadening occurring in TCV and other devices, a better characterization of turbulence is necessary. In particular, one should focus on measuring the relative density fluctuation level around the separatrix, from inner edge to SOL, as it plays a major role in scattering the beam before it reaches its absorption location. Another key parameter to determine is the turbulent correlation length and, as shown in [13, 23], both radial and poloidal correlation lengths are important as they play different roles in the beam broadening. In TCV, different fluctuations diagnostics are being upgraded, such as the tangential phase contrast imaging system [63], and the ability to characterize turbulence will thus significantly improve in the near future.

On the simulation side, one of the main difficulties is to obtain a good estimate of the actual plasma current density in the presence of EC waves. This is mainly due to the uncertainties on the effective charge and, more importantly, on the loop voltage profile. This forces one to choose between two extreme models of current density profile in LUKE: time-asymptotic or frozen current density (see [7, 8] for examples of the frozen current density mode). This could be improved by solving the

electric field diffusion equation from first principles, allowing for the reconstruction of the actual Ohmic electric field profile. This feature has been implemented very recently in LUKE and could be used in a future work. Finally, to improve the coupling between LUKE/C3PO and other wave propagation solvers, a fully 2D ray spreading can be implemented to take into account non-isotropic beam broadening.

Acknowledgments

This work was supported in part by the Swiss National Science Foundation. This work has been carried out within the framework of the EUROfusion Consortium, partially funded by the European Union via the Euratom Research and Training Programme (Grant Agreement No. 101052200 – EUROfusion). The Swiss contribution to this work has been funded by the Swiss State Secretariat for Education, Research and Innovation (SERI). Views and opinions expressed are however those of the author(s) only and do not necessarily reflect those of the European Union, the European Commission or SERI. Neither the European Union nor the European Commission nor SERI can be held responsible for them.

ORCID iDs

J. Cazabonne  <https://orcid.org/0000-0001-7629-1375>
 S. Coda  <https://orcid.org/0000-0002-8010-4971>
 O. Krutkin  <https://orcid.org/0000-0002-9124-2659>
 U. Kumar  <https://orcid.org/0000-0002-3258-8078>

References

- [1] Prater R. 2004 Heating and current drive by electron cyclotron waves *Phys. Plasmas* **11** 2349–76
- [2] Kong M. *et al* 2019 Control of neoclassical tearing modes and integrated multi-actuator plasma control on TCV *Nucl. Fusion* **59** 076035
- [3] Coda S., Alberti S., Blanchard P., Goodman T.P., Henderson M.A., Nikkola P., Peysson Y. and Sauter O. 2003 Electron cyclotron current drive and suprathermal electron dynamics in the TCV tokamak *Nucl. Fusion* **43** 1361–70
- [4] Nikkola P., Sauter O., Behn R., Coda S., Condea I., Goodman T.P., Henderson M.A. and Harvey R.W. (the TCV team) 2003 Modelling of the electron cyclotron current drive experiments in the TCV tokamak *Nucl. Fusion* **43** 1343–52
- [5] Slief J.H., van Kampen R.J.R., Brookman M.W., van Dijk J., Westerhof E. and van Berkel M. 2023 Quantifying electron cyclotron power deposition broadening in DIII-D and the potential consequences for the ITER EC system *Nucl. Fusion* **63** 026029
- [6] Hofmann F. *et al* 1994 Creation and control of variably shaped plasmas in TCV *Plasma Phys. Control. Fusion* **36** B277
- [7] Choi D., Coda S., Decker J., Cazabonne J.A. and Peysson Y. 2020 Study of suprathermal electron dynamics during electron cyclotron current drive using hard x-ray measurements in the TCV tokamak *Plasma Phys. Control. Fusion* **62** 115012
- [8] Cazabonne J. *et al* (the TCV Team) 2023 Experimental and numerical investigations of electron transport enhancement

- by electron-cyclotron plasma-wave interaction in tokamaks *Plasma Phys. Control. Fusion* **65** 104001
- [9] Donnel P., Cazabonne J., Villard L., Brunner S., Coda S., Decker J., Murrugappan M. and Sadr M. 2021 Quasilinear treatment of wave-particle interactions in the electron cyclotron range and its implementation in a gyrokinetic code *Plasma Phys. Control. Fusion* **63** 064001
- [10] Donnel P., Fontana J.-B., Cazabonne J., Villard L., Brunner S., Coda S., Decker J. and Peysson Y. 2022 Electron-cyclotron resonance heating and current drive source for flux-driven gyrokinetic simulations of tokamaks *Plasma Phys. Control. Fusion* **64** 095008
- [11] Bertelli N., Balakin A.A., Westerhof E., Garcia O.E., Nielsen A.H. and Naulin V. 2010 The influence of the edge density fluctuations on electron cyclotron wave beam propagation in tokamaks *J. Phys.: Conf. Ser.* **26** 012002
- [12] Sysoeva E.V., da Silva F., Gusakov E.Z., Heuraux S. and Popov A.Y. 2015 Electron cyclotron resonance heating beam broadening in the edge turbulent plasma of fusion machines *Nucl. Fusion* **55** 033016
- [13] Tretinnikov P., Gusakov E. and Heuraux S. 2021 X-mode beam broadening in turbulent plasma *Plasma Phys. Control. Fusion* **63** 085003
- [14] Tsironis C., Peeters A.G., Isliker H., Strintzi D., Chatziantonaki I. and Vlahos L. 2009 Electron-cyclotron wave scattering by edge density fluctuations in ITER *Phys. Plasmas* **16** 112510
- [15] Hizanidis K., Ram A.K., Kominis Y. and Tsironis C. 2010 Fokker-planck description of the scattering of radio frequency waves at the plasma edge *Phys. Plasmas* **17** 022505
- [16] Peysson Y., Decker J., Morini L. and Coda S. 2011 RF current drive and plasma fluctuations *Plasma Phys. Control. Fusion* **53** 124028
- [17] Decker J., Peysson Y. and Coda S. 2012 Effect of density fluctuations on ECCD in ITER and TCV *EPJ Web Conf.* **32** 01016
- [18] Peysson Y., Decker J. and Morini L. 2012 A versatile ray-tracing code for studying rf wave propagation in toroidal magnetized plasmas *Plasma Phys. Control. Fusion* **54** 045003
- [19] Weber H., Maj O. and Poli E. 2015 Scattering of diffracting beams of electron cyclotron waves by random density fluctuations in inhomogeneous plasmas *EPJ Web Conf.* **87** 01002
- [20] Snicker A., Poli E., Maj O., Guidi L., Köhn A., Weber H., Conway G., Henderson M. and Saibene G. 2017 The effect of density fluctuations on electron cyclotron beam broadening and implications for ITER *Nucl. Fusion* **58** 016002
- [21] Snicker A., Poli E., Maj O., Guidi L., Köhn A., Weber H., Conway G.D., Henderson M. and Saibene G. 2017 Interaction of the electron density fluctuations with electron cyclotron waves from the equatorial launcher in ITER *Plasma Phys. Control. Fusion* **60** 014020
- [22] Köhn A., Guidi L., Holzhauser E., Maj O., Poli E., Snicker A. and Weber H. 2018 Microwave beam broadening due to turbulent plasma density fluctuations within the limit of the born approximation and beyond *Plasma Phys. Control. Fusion* **60** 075006
- [23] Holland L., Köhn-Seemann A. and Vann R.G.L. 2023 Parametric dependence of microwave beam broadening by plasma density turbulence *Nucl. Fusion* **63** 056013
- [24] Ram A.K., Hizanidis K. and Kominis Y. 2013 Scattering of radio frequency waves by blobs in tokamak plasmas *Phys. Plasmas* **20** 056110
- [25] Ioannidis Z.C., Ram A.K., Hizanidis K. and Tigelis I.G. 2017 Computational studies on scattering of radio frequency waves by density filaments in fusion plasmas *Phys. Plasmas* **24** 102115
- [26] Tsironis C., Papagiannis P., Bairaktaris F., Valvis S.I. and Hizanidis K. 2021 Modelling effects of edge density fluctuations on electron-cyclotron current drive used for neoclassical tearing mode stabilization *J. Plasma Phys.* **87** 905870103
- [27] Chellaï O. *et al* 2018 Millimeter-wave beam scattering by field-aligned blobs in simple magnetized toroidal plasmas *Phys. Rev. Lett.* **120** 105001
- [28] Chellaï O. *et al* 2018 Millimeter-wave beam scattering by edge-plasma density fluctuations in TCV *Plasma Phys. Control. Fusion* **61** 014001
- [29] Chellaï O., Alberti S., Furno I., Goodman T., Maj O., Merlo G., Poli E., Ricci P., Riva F. and Weber H. 2021 Millimeter-wave beam scattering and induced broadening by plasma turbulence in the TCV tokamak *Nucl. Fusion* **61** 066011
- [30] Brookman M.W. *et al* 2017 Experimental measurement of ecrh deposition broadening: beyond anomalous transport *EPJ Web Conf.* **147** 03001
- [31] Brookman M.W. *et al* 2021 Resolving ecrh deposition broadening due to edge turbulence in DIII-D *Phys. Plasmas* **28** 042507
- [32] Brookman M.W. *et al* 2023 Broadening of microwave heating beams in the DIII-D tokamak by edge turbulence *Nucl. Fusion* **63** 044001
- [33] Molina Cabrera P., Coda S., Porte L. and Smolders A. 2019 V-band nanosecond-scale pulse reflectometer diagnostic in the TCV tokamak *Rev. Sci. Instrum.* **90** 123501
- [34] Krutkin O., Brunner S. and Coda S. 2023 A method for density fluctuation measurements using pulse reflectometry *Nucl. Fusion* **63** 076012
- [35] Wootton A.J., Carreras B.A., Matsumoto H., McGuire K., Peebles W.A., Ritz C.P., Terry P.W. and Zweben S.J. 1990 Fluctuations and anomalous transport in tokamaks *Phys. Fluids B* **2** 2879-903
- [36] Graves J.P., Horacek J., Pitts R.A. and Hopcraft K.I. 2005 Self-similar density turbulence in the TCV tokamak scrape-off layer *Plasma Phys. Control. Fusion* **47** L1
- [37] Horacek J., Pitts R.A. and Graves J.P. 2005 Overview of edge electrostatic turbulence experiments on TCV *Czech. J. Phys.* **55** 271-83
- [38] Medvedeva A. *et al* 2017 Density profile and turbulence evolution during I-h transition studied with the ultra-fast swept reflectometer on ASDEX upgrade *Plasma Phys. Control. Fusion* **59** 125014
- [39] Rhodes T.L., Leboeuf J.-N., Sydora R.D., Groebner R.J., Doyle E.J., McKee G.R., Peebles W.A., Rettig C.L., Zeng L. and Wang G. 2002 Comparison of turbulence measurements from DIII-D low-mode and high-performance plasmas to turbulence simulations and models *Phys. Plasmas* **9** 2141-8
- [40] Carter T.A. 2006 Intermittent turbulence and turbulent structures in a linear magnetized plasma *Phys. Plasmas* **13** 010701
- [41] Nespoli F., Furno I., Labit B., Ricci P., Avino F., Halpern F.D., Musil F. and Riva F. 2017 Blob properties in full-turbulence simulations of the TCV scrape-off layer *Plasma Phys. Control. Fusion* **59** 055009
- [42] Poli E., Peeters A.G. and Pereverzev G.V. 2001 Torbeam, a beam tracing code for electron-cyclotron waves in tokamak plasmas *Comput. Phys. Commun.* **136** 90-104
- [43] Poli E. *et al* 2018 Torbeam 2.0, a paraxial beam tracing code for electron-cyclotron beams in fusion plasmas for extended physics applications *Comput. Phys. Commun.* **225** 36-46

- [44] Farina D. 2007 A quasi-optical beam-tracing code for electron cyclotron absorption and current drive: gray *Fusion Sci. Technol.* **52** 154–60
- [45] Köhn A., Cappa A., Holzhauer E., Castejón F., Fernández A. and Stroth U. 2008 Full-wave calculation of the O-X-B mode conversion of Gaussian beams in a cylindrical plasma *Plasma Phys. Control. Fusion* **50** 085018
- [46] Williams T.R.N., Köhn A., O'Brien M.R. and Vann R.G.L. 2014 Propagation in 3D of microwaves through density perturbations *Plasma Phys. Control. Fusion* **56** 075010
- [47] Prater R. et al 2008 Benchmarking of codes for electron cyclotron heating and electron cyclotron current drive under ITER conditions *Nucl. Fusion* **48** 035006
- [48] Figini L., Decker J., Farina D., Marushchenko N.B., Peysson Y., Poli E. and Westerhof E. (ITM-TF contributors) 2012 Benchmarking of electron cyclotron heating and current drive codes on ITER scenarios within the European integrated tokamak modelling framework *EPJ Web Conf.* **32** 01011
- [49] COMSOL RF Module User's Guide (version 5.4)
- [50] Bornatici M., Cano R., De Barbieri O. and Engelmann F. 1983 Electron cyclotron emission and absorption in fusion plasmas *Nucl. Fusion* **23** 1153–257
- [51] Westerhof E. 1997 Wave propagation through an electron cyclotron resonance layer *Plasma Phys. Control. Fusion* **39** 1015–29
- [52] Stix T.H. 1992 *Waves in Plasmas* (American Institute of Physics)
- [53] Peysson Y. and Decker J. 2014 Numerical simulations of the radio-frequency-driven toroidal current in tokamaks *Fusion Sci. Technol.* **65** 22–42
- [54] Cazabonne J., Coda S., Decker J. and Peysson Y. 2021 Scattering of electron-cyclotron waves by plasma density fluctuations in tokamaks *Proc. 47th Conf. on Plasma Physics (EPS)(Stiges, Spain, 21–25 June 2021)* (available at: <http://ocs.ciemat.es/EPS2021PAP/pdf/P1.1061.pdf>)
- [55] Lax M., Louisell W.H. and McKnight W.B. 1975 From Maxwell to paraxial wave optics *Phys. Rev. A* **11** 1365–70
- [56] Peysson Y. and Decker J. 2008 Fast electron bremsstrahlung in axisymmetric magnetic configuration *Phys. Plasmas* **15** 092509
- [57] Gnesin S., Coda S., Decker J. and Peysson Y. 2008 Suprathermal electron studies in the TCV tokamak: design of a tomographic hard-x-ray spectrometer *Rev. Sci. Instrum.* **79** 10F504
- [58] Kamleitner J., Coda S., Gnesin S. and Marmillod P. 2014 Comparative analysis of digital pulse processing methods at high count rates *Nucl. Instrum. Methods Phys. Res. A* **736** 88–98
- [59] Choi D., Coda S., Decker J. and Peysson Y. 2020 Modeling of the response function of CdTe detectors for a hard x-ray synthetic diagnostic *Fusion Eng. Des.* **159** 111733
- [60] Cerfon A.J. and Freidberg J.P. 2010 'one size fits all' analytic solutions to the Grad-Shafranov equation *Phys. Plasmas* **17** 032502
- [61] Decker J., Hirvijoki E., Embreus O., Peysson Y., Stahl A., Pusztai I. and Fülöp T. 2016 Numerical characterization of bump formation in the runaway electron tail *Plasma Phys. Control. Fusion* **58** 025016
- [62] Decker J. et al 2023 Recent progress in runaway electron research at TCV *Proc. 29th IAEA Fusion Energy Conf. (FEC)(London, United Kingdom, 16–21 October 2023)*
- [63] Marinoni A., Coda S., Chavan R. and Pochon G. 2006 Design of a tangential phase contrast imaging diagnostic for the TCV tokamak *Rev. Sci. Instrum.* **77** 10E929